

The effects of dilatancy in composite assemblies as micropolar continua*

Farui Shi^{a,b,c}, Nicholas Fantuzzi^{c,*}, Patrizia Trovalusci^d, Yong Li^{a,b} and Zuoan Wei^{a,b}

^aState Key Laboratory of Coal Mine Disaster Dynamics and Control, Chongqing University, Chongqing, China

^bSchool of Resources and Safety Engineering, Chongqing University, Chongqing, China

^cDICAM Department, University of Bologna, Italy

^dDISG Department, Sapienza University of Rome, Italy

ARTICLE INFO

Keywords:

dilatancy
micropolar theory
rough micro-structure
homogenization procedure
contact density model

ABSTRACT

Dilatancy is of importance for understanding the micromechanical behavior of materials such as cemented sand, mortar joints, and the interfaces of masonry-like structures. Rough interface contacts are able to result in dilatancy and lead to an increase in the material's volume. However, as far as the authors' knowledge very few works are present regarding such phenomenon in composite materials. The present work aims at investigating the effect of dilatancy on composite materials with rigid particles connected by rough elastic interfaces. Different hexagonal shapes as rigid particles are considered by a series of geometric parameters. The stiffness properties of the rough interface can be obtained by employing a statistical distribution function of the roughness termed contact density model. A homogenization procedure based on an energetic equivalence criterion is used to derive the constitutive parameters. The homogenized continuum results to be a micropolar continuum with an additional degree of freedom (the microrotation) and is known to be able to give an effective result in modeling the behavior of materials with micro-structures. A 2D plane slope composed of material with various roughness interfaces is analyzed under the effect of dilatancy. This study shows the validity of the micropolar theory when considering the rough microstructure, which is essential for capturing more realistic behavior of composite materials.

1. Introduction


The presence of internal microstructures such as joints, cracks, and voids can complicate the studies on composite materials, especially for the microstructure with rough interfaces. Rough interfaces are able to induce a dilatancy effect, namely bring coupling between normal and shear behavior, under load applied [1, 2]. The dilatancy effect has been studied in granular materials [3, 4, 5], rock joints [2, 6, 7], mortar joints and brick-mortar interfaces [8] and porous materials [9, 10]. However, there is scarce attention paid to the effect of dilatancy on composite materials, since it may affect the macroscopic mechanical behavior.


Understanding the behavior of the microstructure especially with a rough interface is of importance in the study of composite materials. Discrete element models in general can accurately predict the mechanical behavior of complex materials, but this approach requires a huge computational cost [11, 12]. Alternatively, homogenizing such materials as an equivalent continuum can provide fast and satisfactory results [13, 14, 15]. However, the successful application of such approach needs to select proper continuum theory and homogenization method, transforming heterogeneous materials to equivalent continua [16, 17, 18, 19, 20, 21].

When dealing with microstructured materials in which the internal lengths are not negligible compared to the structural length scale, it is well-known that the classical and local Cauchy (grade 1) continuum is not able to satisfactorily describe the real mechanical behavior of materials and can result in ill-posed problems. That is because

*The results of this research have been partially presented at the 7th International Conference on Mechanics of Composites, 1–3 September 2021, Porto, Portugal.

*Corresponding author

 farui.shi@unibo.it (F. Shi); nicholas.fantuzzi@unibo.it (N. Fantuzzi); patrizia.trovalusci@uniroma1.it (P. Trovalusci); yong.li@cqu.edu.cn (Y. Li); weiza@cqu.edu.cn (Z. Wei)

 <https://www.unibo.it/sitoweb/nicholas.fantuzzi/en> (N. Fantuzzi);
<https://sites.google.com/a/uniroma1.it/multiscale-and-multiphysics-modelling-for-complex-materials/> (P. Trovalusci)

ORCID(s): 0000-0002-8406-4882 (N. Fantuzzi); 0000-0001-7946-3590 (P. Trovalusci)

this continuum ignores the internal length parameter. However, the mechanical properties for rough interfaces can vary with scale [22, 23]. Therefore, non-classical and non-local continuum which can retain memory of the internal structure of the material at a fine scale needed to be developed [24, 25]. In general, the non-local description can be in two different ways [26, 27, 28]: the first is named explicit/strong non-local description obtained by adding extra parameters to account for the non-locality of material. This description does not change the classical kinematics and introduced the evaluation of stress in proper neighborhood of the material points [29, 30, 31]; the second can be named implicit/weak non-local description obtained by adding extra degrees of freedom. Among implicit non-local continua, the micropolar continua can be included. Non-local models have been satisfactorily used for studies on composite materials because they reveal microstructures that can influence macroscopic mechanical behaviors [32, 33, 34]. Non-local models allows to properly take into account size effects [15, 16, 17, 28, 35, 36, 37, 38, 39, 40].

The homogenization process is able to provide more reliable models when the classical continuum is equipped with additional degrees of freedom (i.e. as the the implicit/weak non-local continua) [9, 26, 27, 28, 41, 42, 43]. A peculiar strain measure of the micropolar model is the relative rotation between the macrorotation and microrotation that can be used to investigate the micropolar effect. In the work [44], in agreement with the literature [45, 46, 47] it has been shown that the micropolar effect is more evident when geometrical or load singularities exist such as concentrated loads and holes.

For the microstructure with a rough interface, such as rough micro-cracks, dilatancy is needed to be considered when analyzing the mechanical properties of materials. Many studies have demonstrated that roughness plays an essential role in the interface behavior [6, 48, 49, 50]. On the contrary, for smooth interfaces, sliding dominates the mechanism of shear. As the roughness of interface increases, interlocking and dilatancy could happen [51]. When the volume of interface is constrained, the dilatancy can increase the normal stresses acting on the interface, which can increase resistance of the interface [52]. Moreover, it was found that the shear behavior of the interface depends on the roughness. Rough interfaces show a higher shear strength than smooth interfaces [53]. That is because the rougher interfaces own higher interlocking that can mobilize strength of the contact material and thus they result to be more resistant to shear [54]. The higher shear strength of rough interface can be also observed experimentally in previous studies [48, 55, 56].

Based on a discrete (crack) interface with interlocking, several dilatancy models had been developed. Baggio and Trovalusci [57] considered dilatancy for the analysis of friction in brick-block masonry structures. Bažant and Gambarova [58] proposed a rough crack model which considered interfaces as triangular or saw-tooth asperity surface. By optimizing the fits of test results, stiffness coefficients including dilatancy stiffness of this model can be obtained as a function of tractions and displacement in normal and shear directions. As an improvement of the above model, Gambarova and Karakoç [59] illustrated a better formulation for the relation between tractions and displacements. The above models can be denoted as empirical models because they are based on experimental results and have empirical formulations. Physical dilatancy models had also been proposed by assuming the shape of the rough interface. Two representative physical dilatancy models can be the two-phase model by Walraven [60] and the contact density model by Li et al. [61]. For modeling purposes, the contact density model is used in this paper to study the dilatancy effect of rough interfaces. The detailed application of this model can be seen in Section 2.1.

The present work aims to investigate the dilatancy effect on composite materials made of hexagonal particles and rough elastic interfaces. The dilatancy can result from the rough interface, of which the roughness is obtained by assuming a density function for the interface shape. Three hexagonal geometries termed regular, hourglass, and asymmetric are considered by changing geometry parameters of regular hexagon but keeping equal side length. 2D composite assembly is homogenized as a micropolar continuum according to an energetic equivalence introduced for the first time in [16]. Since the present homogenization consider the internal length scale, such effect is investigated by selecting different scales of the particles. The simulations are performed on a slope case under load on a limited area, using a standard finite element method based on the micropolar theory, with mixed interpolation functions for the displacement (quadratic) and rotation (linear) fields. The results are presented in graphical form for displacements, stresses, and relative rotation.

This work is structured as follows. After the introduction section, the methodology used in this paper is illustrated in Section 2. Section 2.1 introduces the dilatancy model applied on rough interfaces and derives the formulations of interface stiffness. Section 2.2 presents micropolar continuum model and introduces current quantities and symbols. Section 2.3 gives the numerical finite element method for the micropolar continuum. Geometries of microstructured composites are introduced in Section 2.4. Numerical simulations are presented in Section 3. Roughness and stiffness matrices of interfaces are determined in Section 3.1. Section 3.2 reports the constitutive matrices of different RVEs for

both micropolar and Cauchy models. Section 3.3 illustrates the numerical applications of a 2D slope case subjected to loads and boundary conditions with different material configurations. Finally, conclusions and remarks are drawn in Section 4.

2. Methodology

2.1. Dilatancy model

A rough interface in open state is able to transmit a significant amount of shear (aggregate interlock) [62]. This is accompanied by dilatancy, which implies that when displacement is introduced along an open interface, not only shear stress but also normal compressive stress are induced accompanied by the opening of the interface. Now consider an open interface that is planar but microscopically rough as shown in Fig. 1. The interface constitutive relation can be expressed as a function of total relative displacements [58]:

$$\mathbf{t} = \mathcal{F}(\mathbf{u}) \quad (1)$$

where \mathcal{F} represents the vector of generic functions of the relative displacements to be defined according to the selected model, $\mathbf{t}^\top = [t_n \ t_t]$ is the interface stress vector and $\mathbf{u}^\top = [\Delta u_n \ \Delta u_t]$ collects the relative displacements, where subscripts n and t represent normal and tangential components. In the following function \mathcal{F} is specified for a particular case based on experimental evidence.

This relation (1) is assumed to be linear:

$$\mathbf{t} = \mathbf{K}\mathbf{u} \quad (2)$$

where \mathbf{K} indicates the stiffness matrix of the rough interface and the stiffness coefficients can be defined by:

$$\mathbf{K} = \mathbf{t} \left(\frac{\partial}{\partial \mathbf{u}} \right)^\top \quad (3)$$

Li et al. [61] proposed a successful physical crack-dilatancy model called contact density model. In this model, the roughness of a crack surface is idealized as a collection of segments (called contact units) each with a given inclination ($\theta \in [-\pi/2, \pi/2]$) with respect to a horizontal crack plane. The overall distribution of these inclinations can be described by a contact density function. The contact stresses are proposed to be fixed and act perpendicular to the individual contact planes. This model is based on three assumptions:

- The density function $\Omega(\theta)$ is assumed as a trigonometric function independent on the size, the grading and the strength of the interface aggregates.
- The contact stress is computed with a elastic-perfectly plastic model for the contact stress prediction σ_{con} . As pointed out in previous studies [1], some friction is likely to be present. Therefore, shear contact pressure σ_{she} is also considered.
- When the normal displacement Δu_n is larger enough than the surface roughness, an effective ratio of contact area $H(\Delta u_n)$ represents the loss of contact area.

By transforming the contact pressures from the local coordinate to global coordinate, interface constitutive equation (1) becomes:

$$\mathbf{t} = \int_{-\pi/2}^{\pi/2} \begin{bmatrix} \cos \theta & -\sin \theta \\ \sin \theta & \cos \theta \end{bmatrix} \begin{bmatrix} \sigma_{\text{con}}(\mathbf{u}) \\ \sigma_{\text{she}}(\mathbf{u}) \end{bmatrix} H(\Delta u_n) A_t \Omega(\theta) d\theta \quad (4)$$

where A_t represents the ratio between the interface area and sectional area of the interface plane, that in the following will be considered to be related to $\Omega(\theta)$ as:

$$A_t = \left[\int_{-\pi/2}^{\pi/2} \Omega(\theta) \cos \theta d\theta \right]^{-1} \quad (5)$$

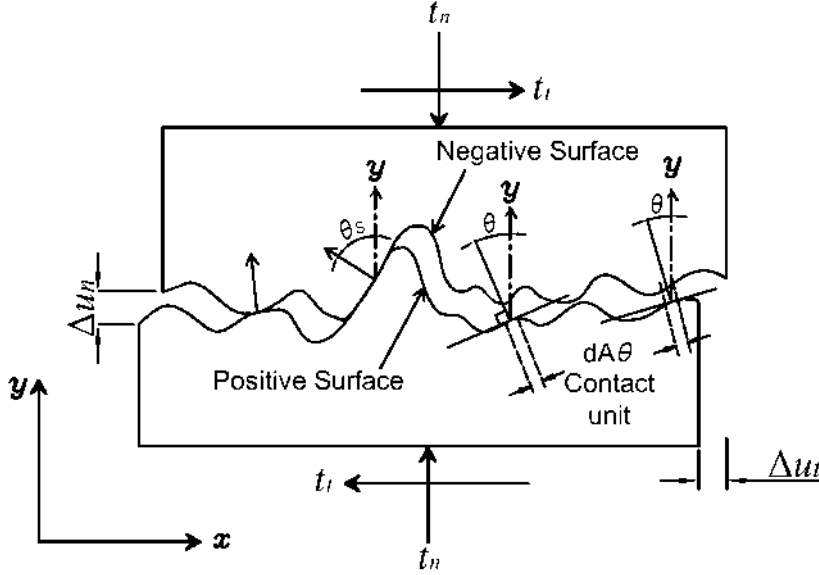


Figure 1: Sketch of rough crack surface including definitions and notations in the contact density model.

The effective ratio of contact area $H(\Delta u_n)$ can be expressed by an exponential function:

$$H(\Delta u_n) = 1 - \exp\left(1 - \frac{0.5G_{\max}}{\Delta u_n}\right) \geq 0 \quad (6)$$

where G_{\max} is the maximum aggregate size present at the material interface.

Please note that, the compressive stress t_n and the closing displacement Δu_n are defined as positive, whereas the shear stress and shear displacement are defined to be positive when the negative side of the contact plane (see Fig. 1) moves towards the positive direction of the x axis.

In the following the contact density function $\Omega(\theta)$ takes the trigonometric form:

$$\Omega(\theta) = A_\Omega \cos \theta \quad (7)$$

at the same time the relation below should be satisfied according to Li et al. [61]:

$$\int_{-\pi/2}^{\pi/2} \Omega(\theta) d\theta = 1 \quad (8)$$

For instance, if $A_\Omega = 0.5$ thus $A_t = 1.27$ in order to satisfy Eq. (8), which means that the surface area is 1.27 times of the sectional area of the interface.

The contact compressive σ_{con} and shear σ_{she} stresses acting on the crack interface is calculated using an elastic-plastic constitutive law [61] expressed by

$$\sigma_{\text{con}} = R_s \omega_\theta, \quad \sigma_{\text{she}} = R_t \delta_\theta \quad (9)$$

where R_s and R_t are elastic rigidities per unit of length. According to Li et al. [61]:

$$R_s = A_s f_c^\alpha, \quad R_t = \eta R_s, \quad \text{for } \eta = G/E \quad (10)$$

where η is the ratio between shear and normal stiffness (generally between 1/3 or 1/2 for known values of Poisson ratio for granular materials) and A_s and α are coefficients to be carried by experimental testing. f_c is the compressive strength of the joint (e.g. concrete, rocks, etc.). ω_θ and δ_θ are local normal and tangential displacements of the contact surface. The coordinate transformation relation of displacements are:

$$\begin{aligned} \omega_\theta &= \Delta u_n \cos \theta + \Delta u_t \sin \theta \\ \delta_\theta &= \Delta u_n (-\sin \theta) + \Delta u_t \cos \theta \end{aligned} \quad (11)$$

From the above mentioned, the constitutive relation can be carried out by the contact density model (4), as well as the stiffness matrix for open cracks with different roughness. The roughness is decided by three terms in the model [1]:

- G_{\max} , the maximum size of aggregate. Larger aggregate sizes can correspond to higher roughness indexes.
- A_t , when $A_t \approx 1$ interface is almost flat whereas higher values (recorded up to approximately 1.30) indicate rougher surfaces.
- $\Omega(\theta)$, the contact density function, represents the distribution of unit surface direction. The direction distribution has a larger density in the directions near $\pm\pi/2$ corresponding to the steeper direction or higher roughness of the surface.

It should be noted that there is a relationship between G_{\max} and f_c . The change in G_{\max} may also induce a change in f_c . In any case, approaches for estimating the surface roughness only based on the maximum aggregate size G_{\max} should be improved by also accounting for the influence of the surface strength [1]. But as suggested by Li et al. [61], since the maximum size of coarse aggregate is much larger than the interface width, it is reasonable to presume the effective ratio of contact area to be negligible. The value of $H(\Delta u_n)$ can be simplified to be unity. It can also be seen that A_t is actually a function of $\Omega(\theta)$ (Eq. 5). Therefore, the effect of roughness can be investigated under different $\Omega(\theta)$.

Here, contact surfaces with different roughness can be defined by considering different contact density functions $\Omega(\theta)$. According to Eq. (4), the constitutive relations become:

$$\begin{aligned} t_n &= \int_{\theta}^{\pi/2} (\sigma_{\text{con}} \cos \theta - \sigma_{\text{she}} \sin \theta) A_t \Omega(\theta) d\theta \\ t_t &= \int_{\theta}^{\pi/2} (\sigma_{\text{con}} \sin \theta + \sigma_{\text{she}} \cos \theta) A_t \Omega(\theta) d\theta \end{aligned} \quad (12)$$

where θ is an angular parameter that can be set $\theta \in [-\pi/2, 0]$ and $A_t \in [1, 1.3]$. The stiffness coefficients are:

$$\begin{aligned} K_{11} &= \int_{\theta}^{\pi/2} \left(\frac{\partial \sigma_{\text{con}}}{\partial \Delta u_n} \cos \theta - \frac{\partial \sigma_{\text{she}}}{\partial \Delta u_n} \sin \theta \right) A_t \Omega(\theta) d\theta \\ K_{12} &= \int_{\theta}^{\pi/2} \left(\frac{\partial \sigma_{\text{con}}}{\partial \Delta u_t} \cos \theta - \frac{\partial \sigma_{\text{she}}}{\partial \Delta u_t} \sin \theta \right) A_t \Omega(\theta) d\theta \\ K_{21} &= \int_{\theta}^{\pi/2} \left(\frac{\partial \sigma_{\text{con}}}{\partial \Delta u_n} \sin \theta + \frac{\partial \sigma_{\text{she}}}{\partial \Delta u_n} \cos \theta \right) A_t \Omega(\theta) d\theta \\ K_{22} &= \int_{\theta}^{\pi/2} \left(\frac{\partial \sigma_{\text{con}}}{\partial \Delta u_t} \sin \theta + \frac{\partial \sigma_{\text{she}}}{\partial \Delta u_t} \cos \theta \right) A_t \Omega(\theta) d\theta \end{aligned} \quad (13)$$

where K_{11} , K_{22} , and K_{12} are respectively the normal, shear and dilatancy stiffness of the interface. Then considering Eq. (9), Eq. (13) becomes:

$$\begin{aligned} K_{11} &= \int_{\theta}^{\pi/2} (R_s \cos^2 \theta + R_t \sin^2 \theta) A_t \Omega(\theta) d\theta \\ K_{12} &= \int_{\theta}^{\pi/2} (R_s - R_t) \sin \theta \cos \theta A_t \Omega(\theta) d\theta \\ K_{21} &= \int_{\theta}^{\pi/2} (R_s - R_t) \cos \theta \sin \theta A_t \Omega(\theta) d\theta \\ K_{22} &= \int_{\theta}^{\pi/2} (R_s \sin^2 \theta + R_t \cos^2 \theta) A_t \Omega(\theta) d\theta \end{aligned} \quad (14)$$

where clearly $K_{12} = K_{21}$ so the stiffness matrix is symmetric as expected. By considering Eq. (10), finally:

$$\begin{aligned} K_{11} &= \int_{\theta}^{\pi/2} A_s f_c^\alpha (\cos^2 \theta + \eta \sin^2 \theta) A_r \Omega(\theta) d\theta \\ K_{12} &= \int_{\theta}^{\pi/2} \eta A_s f_c^\alpha \sin \theta \cos \theta A_r \Omega(\theta) d\theta \\ K_{22} &= \int_{\theta}^{\pi/2} A_s f_c^\alpha (\sin^2 \theta + \eta \cos^2 \theta) A_r \Omega(\theta) d\theta \end{aligned} \quad (15)$$

As suggested by Li et al. [61], the contact units are in directions from $\theta = \arctan \frac{\Delta u_n}{\Delta u_t}$ to $\pi/2$. The region with directions from $-\pi/2$ to $\theta = \arctan \frac{\Delta u_n}{\Delta u_t}$ give no contribution to the contact force. As $\Delta u_n, \Delta u_t > 0$, the integral range should be within $[0, \pi/2]$.

2.2. Micropolar continuum

The micropolar (i.e. Cosserat) continuum has shown a good implementation in the investigation of mechanical behavior of microstructures [63, 64, 17]. This continuum, according to [28], belongs to the implicit non-local continuum theories since it considers the microrotation of the material particles in addition to the classical (Cauchy continuum) displacement field. For the sake of simplicity, a 2D framework of the micropolar continuum is considered in this study. Therefore, there are three degrees of freedom (DOFs) for each material particle, i.e. two macro-displacements u_1, u_2 and one microrotation ω . By assuming a linearized kinematics, the kinematic compatibility equations can be written as:

$$\varepsilon_{11} = u_{1,1}, \quad \varepsilon_{22} = u_{2,2}, \quad \varepsilon_{12} = u_{1,2} + \omega, \quad \varepsilon_{21} = u_{2,1} - \omega, \quad \chi_1 = \omega_{,1}, \quad \chi_2 = \omega_{,2} \quad (16)$$

where ε_{ij} ($i, j = 1, 2$) are the components of the strain tensor and χ_i ($i = 1, 2$) are the micropolar curvatures, subscripts $_{,1}$ and $_{,2}$ stand for the partial derivatives with respect to $x_1 = x$ and $x_2 = y$. It should be noticed that in the micropolar model, the tangential strain components are not reciprocal, $\varepsilon_{12} \neq \varepsilon_{21}$. Note that, the microrotation (ω) in this model is different from the local rigid rotation (macrorotation, ϑ), which is defined as the skew-symmetric part of the gradient of displacement $\vartheta = 0.5(u_{2,1} - u_{1,2})$. The difference between macrorotation and microrotation ($\vartheta - \omega$), named as relative rotation, can be a measurement to investigate the effect of the micropolar model.

The work conjugate stress and microcouple measurements σ_{ij} and μ_i for $i, j = 1, 2$ to ε_{ij} and χ_i , respectively. The stress components are not reciprocal, $\sigma_{12} \neq \sigma_{21}$. The stresses and microcouples should satisfy the equilibrium at external boundary. Therefore, the surface traction t_i and moment traction m_i can be expressed as $t_i = \sigma_{ij} n_j$ and $m_i = \mu_j n_j$, respectively. where n_j is the components of the outward normal to the boundary. From the virtual work principle, balance equations can be carried out:

$$\sigma_{i,j,j} + b_i = 0, \quad \mu_{j,j} - e_{ij3} \sigma_{ij} = 0 \quad (17)$$

where b_i are the body force components, e_{ij3} is the permutation tensor. The linear 2D micropolar stress-strain relations can be written in matrix form as:

$$\begin{Bmatrix} \sigma_{11} \\ \sigma_{22} \\ \sigma_{12} \\ \sigma_{21} \\ \mu_1 \\ \mu_2 \end{Bmatrix} = \begin{bmatrix} A_{1111} & A_{1122} & A_{1112} & A_{1121} & B_{111} & B_{112} \\ A_{2211} & A_{2222} & A_{2212} & A_{2221} & B_{221} & B_{222} \\ A_{1211} & A_{1222} & A_{1212} & A_{1221} & B_{121} & B_{122} \\ A_{2111} & A_{2122} & A_{2112} & A_{2121} & B_{211} & B_{212} \\ B_{111} & B_{122} & B_{112} & B_{121} & D_{11} & D_{12} \\ B_{211} & B_{222} & B_{212} & B_{221} & D_{21} & D_{22} \end{bmatrix} \begin{Bmatrix} \varepsilon_{11} \\ \varepsilon_{22} \\ \varepsilon_{12} \\ \varepsilon_{21} \\ \chi_1 \\ \chi_2 \end{Bmatrix} \quad (18)$$

In the case of hyperelastic materials, the above constitutive matrix shows major symmetries as: $A_{ijhk} = A_{hki j}$, $B_{ijh} = B_{hij}$, $D_{ij} = D_{ji}$ ($i, j, h, k = 1, 2$). The symbols $A_{ijhk} = A_{hki j}$, $B_{ijh} = B_{hij}$, and $D_{ij} = D_{ji}$ can be collected in the matrices \mathbb{A} , \mathbb{B} , and \mathbb{D} . Thus, the constitutive relation can be presented in a compact form as:

$$\begin{Bmatrix} \boldsymbol{\sigma} \\ \boldsymbol{\mu} \end{Bmatrix} = \begin{bmatrix} \mathbb{A} & \mathbb{B} \\ \mathbb{B}^T & \mathbb{D} \end{bmatrix} \begin{Bmatrix} \boldsymbol{\varepsilon} \\ \boldsymbol{\chi} \end{Bmatrix} \quad (19)$$

where the stress and microcouple components in the vectors:

$$\boldsymbol{\sigma}^\top = \{\sigma_{11} \quad \sigma_{22} \quad \sigma_{12} \quad \sigma_{21}\}, \quad \boldsymbol{\mu}^\top = \{\mu_1 \quad \mu_2\} \quad (20)$$

similarly, the strain and micropolar curvature components are ordered as:

$$\boldsymbol{\varepsilon}^\top = \{\varepsilon_{11} \quad \varepsilon_{22} \quad \varepsilon_{12} \quad \varepsilon_{21}\}, \quad \boldsymbol{\chi}^\top = \{\chi_1 \quad \chi_2\} \quad (21)$$

2.3. Finite element implementation

The 2D micropolar linear elasticity problem can be solved by a standard displacement-based finite element method. The displacement and rotation components in the micropolar model are ordered as:

$$\mathbf{u}^\top = \{u_1 \quad u_2\}, \quad \boldsymbol{\omega} = \{\omega\}, \quad \mathbf{d}^\top = \{\mathbf{u} \quad \boldsymbol{\omega}\} \quad (22)$$

Based on the virtual work principle, the weak form of the current problem within a domain A and boundary Γ can be written as follows to implement the finite element method,

$$\int_A \delta \boldsymbol{\varepsilon}^\top \boldsymbol{\sigma} + \delta \boldsymbol{\chi}^\top \boldsymbol{\mu} \, dA = \int_A \delta \mathbf{u}^\top \mathbf{b} \, dA + \int_\Gamma \delta \mathbf{u}^\top \bar{\mathbf{t}} + \delta \boldsymbol{\omega}^\top \bar{\mathbf{m}} \, d\Gamma \quad \forall \delta \mathbf{u}, \delta \boldsymbol{\omega} \quad (23)$$

where δ is the variational operator, \mathbf{b} is the body force vector. $\bar{\mathbf{t}}$ and $\bar{\mathbf{m}}$ are the traction and couple-traction vectors applied on the boundary Γ .

It should be noted that lagrangian shape functions can be adopted because the number of equations is equal to the number of kinematic parameters [65]. The displacement and microrotation fields can be approximated by interpolation functions as

$$\mathbf{u} = \mathbf{N}_u \tilde{\mathbf{u}}, \quad \boldsymbol{\omega} = \mathbf{N}_\omega \tilde{\boldsymbol{\omega}} \quad (24)$$

where \mathbf{N}_u and \mathbf{N}_ω are the matrices of lagrangian shape functions for \mathbf{u} and $\boldsymbol{\omega}$. $\tilde{\mathbf{u}}$ and $\tilde{\boldsymbol{\omega}}$ are nodal displacement and microrotation values of each element, respectively. In the present study, in order to avoid element locking, different shape functions are considered for displacement and microrotation [40], i.e. bi-quadratic shape functions for displacements and bi-linear shape functions for microrotations. Nine-node quadrangular elements are used in this study, thus, the displacements at any point of element is approximated by values at all nine nodes, while the microrotation by values at four corner nodes. The shape functions can be expressed in matrix form as:

$$\mathbf{N}_u = \begin{bmatrix} N_1^u & 0 & \dots & N_9^u & 0 \\ 0 & N_1^u & 0 & \dots & N_9^u \end{bmatrix}, \quad \mathbf{N}_\omega = [N_1^\omega \quad \dots \quad N_4^\omega] \quad (25)$$

where classical quadratic and linear shape functions are considered, respectively. The micropolar strains in Eq. (16) can be given by:

$$\boldsymbol{\varepsilon} = \mathbf{L}\mathbf{u} + \mathbf{M}\boldsymbol{\omega}, \quad \boldsymbol{\chi} = \nabla \boldsymbol{\omega} \quad (26)$$

where, ∇ is the gradient operator, \mathbf{L} and \mathbf{M} can be expressed as:

$$\mathbf{L} = \begin{bmatrix} \frac{\partial}{\partial x_1} & 0 & \frac{\partial}{\partial x_2} & 0 \\ 0 & \frac{\partial}{\partial x_2} & 0 & \frac{\partial}{\partial x_1} \end{bmatrix}^\top, \quad \mathbf{M} = [0 \quad 0 \quad 1 \quad -1]^\top \quad (27)$$

Substituting Eq. (24) into Eq. (26), we can obtain:

$$\boldsymbol{\varepsilon} = [\mathbf{L}\mathbf{N}_u \quad \mathbf{M}\mathbf{N}_\omega] \{\tilde{\mathbf{u}} \quad \tilde{\boldsymbol{\omega}}\}^\top = \mathbf{B}_\varepsilon \mathbf{d}, \quad \boldsymbol{\chi} = [0 \quad \nabla \mathbf{N}_\omega] \{\tilde{\mathbf{u}} \quad \tilde{\boldsymbol{\omega}}\}^\top = \mathbf{B}_\chi \mathbf{d} \quad (28)$$

where \mathbf{d} is the unknown vector of nodal displacements. \mathbf{B}_ε and \mathbf{B}_χ represent the matrices including the derivatives of the shape functions. Consequently, the constitutive relations Eq. (18) can be expressed as:

$$\boldsymbol{\sigma} = \mathbb{A}\mathbf{B}_\varepsilon \mathbf{d} + \mathbb{B}\mathbf{B}_\chi \mathbf{d}, \quad \boldsymbol{\mu} = \mathbb{B}^\top \mathbf{B}_\varepsilon \mathbf{d} + \mathbb{D}\mathbf{B}_\chi \mathbf{d} \quad (29)$$

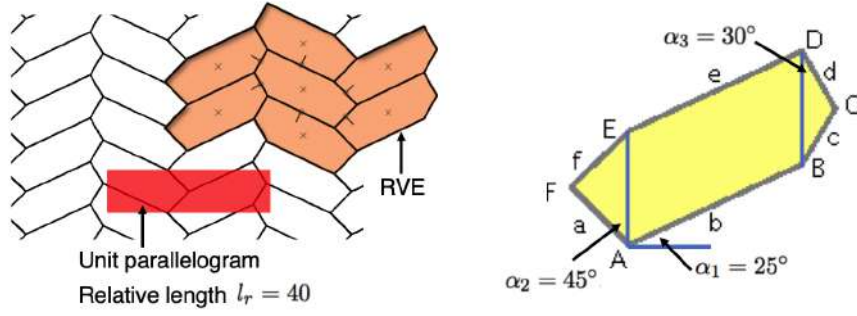


Figure 2: General hexagonal assembly with RVE and single particle with geometric parameters $\alpha_1 = 25^\circ, \alpha_2 = 45^\circ, \alpha_3 = 30^\circ, l_r = 40$.

Note that matrix \mathbb{B} accounts for the coupling between classical and micro-polar effects. Finally, the weak form Eq. (23) (by excluding body forces) of the present micropolar problem becomes:

$$\delta \mathbf{d}^T \int_{\mathcal{A}^e} \underbrace{\left(\mathbf{B}_\varepsilon^T \mathbb{A} \mathbf{B}_\varepsilon + \mathbf{B}_\varepsilon^T \mathbb{B} \mathbf{B}_\chi + \mathbf{B}_\chi^T \mathbb{B}^T \mathbf{B}_\varepsilon + \mathbf{B}_\chi^T \mathbb{D} \mathbf{B}_\chi \right)}_{\mathbf{K}^e} d\mathcal{A}^e \mathbf{d} = \delta \mathbf{d}^T \int_{\Gamma^e} \underbrace{\begin{bmatrix} \mathbf{N}_u^T \bar{\mathbf{t}} \\ \mathbf{N}_\omega^T \bar{\mathbf{m}} \end{bmatrix}}_{\mathbf{F}^e} d\Gamma^e \quad \forall \delta \mathbf{d} \quad (30)$$

where \mathbf{K}^e and \mathbf{F}^e represent the stiffness matrix and the nodal force vector of the adopted finite element for describing a 2D linearly elastic micropolar body. The integral terms in Eq. (30) are computed by a classical Gauss-Legendre integration with 3×3 grid. The solution is carried out by a classic Gauss elimination algorithm after a standard finite element assembly procedure.

The above finite element method is implemented in an in-house finite element MATLAB code which has been developed as an extension of a classical 2D Cauchy continuum as presented in [65].

2.4. Microstructure geometry

In this study, the equivalent micropolar model is considered to be made by hexagonal particles interacting by rough elastic interfaces (microstructures). 7-blocks representative volume element (RVE) is selected as it gives more accurate results than 4-blocks RVE [66]. As shown in Fig. 2, the single hexagonal particle is made of a parallelogram and two isosceles triangles with the base attached to the two shortest opposite sides of the parallelogram as presented in [64]. A general hexagon can be defined by a series of geometric parameters: three angle $\alpha_1, \alpha_2, \alpha_3$, the relative length l_r defined as the ratio between the length of AE (or BD) and the perpendicular distance between AE and BD , and the particle scale s . From Fig. 2, the nodal coordinates of the single hexagon are: $A = (0, 0), B = (l_1, t), C = (l_1 + l_5, t + l_2/2), D = (l_1, t + l_2), E = (0, l_2), F = (-l_4, l_2/2)$, where $l_2 = s(l_r/100), l_1 = s - l_2, t = l_1 \tan \alpha_1, l_4 = (l_2/2) \tan \alpha_2, l_5 = (l_2/2) \tan \alpha_3$.

In the following simulations, three hexagonal patterns termed regular, hourglass, and asymmetric are considered by fixing $\alpha_1 = 0^\circ, l_r = 100/(1/\sqrt{3} + 1)$ and changing the below parameters as:

1. Regular: $\alpha_2 = \alpha_3 = 30^\circ$,
2. Hourglass: $\alpha_2 = \alpha_3 = -20^\circ$,
3. Asymmetric: $-\alpha_2 = \alpha_3 = 30^\circ$.

In the micropolar model, the mechanical behavior of microstructures can be retained by using the procedure introduced in [16]. In order to investigate the effect of scale effect of microstructures, three scales are considered for all three hexagonal RVE as $s = 1.0, 0.5, 0.25$.

3. Numerical simulation

3.1. Roughness and stiffness

Contact density functions with different roughness (A_i) can be constructed based on the density function proposed in Eq. (7) to investigate the effect of dilatancy. Note that all these density functions satisfy the condition indicated in Eq. (8). Following the form in Eq. (7), a general cosine-style contact density function can be formulated as:

$$\Omega(\theta) = \lambda \cos(\beta\theta) \quad (31)$$

where λ and β are coefficients. According to Eq. (8), Eq. (31) satisfies:

$$\int_{-a}^a \lambda \cos(\beta\theta) d\theta = 1 \quad (32)$$

where the inclination angle θ has to be distributed within the indicated domain with $a \in [0, \pi/2]$. By solving Eq. (32), we can obtain $a = \arcsin(\beta/2\lambda)/\beta$, thus, β should belong to $[-2\lambda, 2\lambda]$. It can be seen that β and a are both functions of λ . Here we set $\beta = 2\lambda$, therefore $a = \pi/4\lambda$. By selecting $\lambda = 5, 0.8, 0.7, 0.6, 0.5$, respectively, the selected contact density functions are given below:

$$\begin{aligned} \Omega_1(\theta) &= 5 \cos(10\theta), & |\theta| &\leq \frac{\pi}{20} \\ \Omega_2(\theta) &= 0.8 \cos(1.6\theta), & |\theta| &\leq \frac{\pi}{3.2} \\ \Omega_3(\theta) &= 0.7 \cos(1.4\theta), & |\theta| &\leq \frac{\pi}{2.8} \\ \Omega_4(\theta) &= 0.6 \cos(1.2\theta), & |\theta| &\leq \frac{\pi}{2.4} \\ \Omega_5(\theta) &= 0.5 \cos \theta, & |\theta| &\leq \frac{\pi}{2} \end{aligned} \quad (33)$$

where not indicated, the functions are equal to zero, thus, they cannot take negative values. A graphical representation of these functions can be found in Fig. 3. We can observe that the function $\Omega_5(\theta)$ occupies more angles close to $\pm\pi/2$, which indicates a more rough interface. $\Omega_1(\theta)$ occupies angles very close the 0, representing a nearly smooth interface.

The stiffness matrices can be obtained from Eq. (15) by assuming the integral region as $[0, \pi/2]$ for each continuous function and the following parameters $A_s = 343$, $f_c = 38$, $\alpha = 1/3$, and $\eta = 1/2$. The results are listed in Table 1.

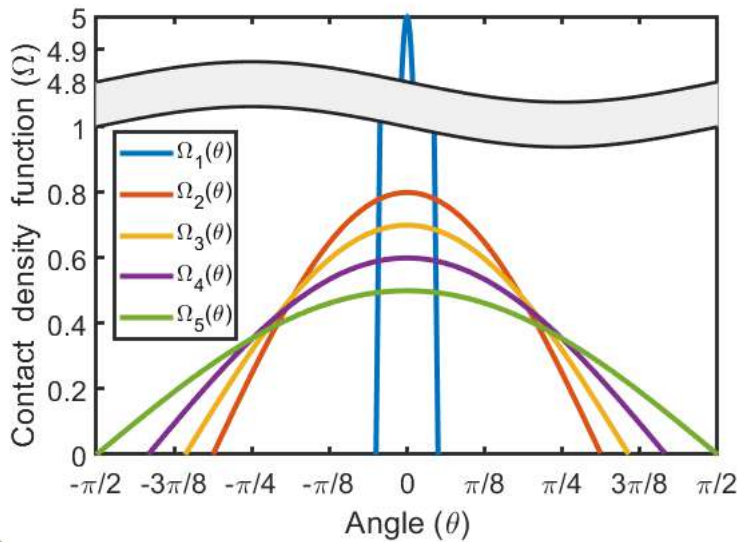


Figure 3: Graphical representation of the selected contact density functions.

Table 1

Roughness and stiffness values for different contact density functions Eq. (33).

	A_r	K_{11}	K_{12}	K_{22}
Ω_1	1.0023	576.58	16.407	290.31
Ω_2	1.0968	581.88	91.664	366.75
Ω_3	1.1289	585.64	101.11	390.68
Ω_4	1.1806	593.42	111.68	427.62
Ω_5	1.2732	611.77	122.35	489.42

Table. 1 lists the roughness and stiffness results of the different selected contact density functions. It can be seen that A_r shows an increasing trend from Ω_1 to Ω_5 . Ω_5 brings the roughest interface, while the roughness of the Ω_1 is very close to 1. Thus, the interface brought by this function could be regarded as a smooth surface. Moreover, we can also observe that the dilatancy stiffness (K_{12}) variation cannot be considered for fixed values of K_{11} and K_{22} by this model. In fact, all four stiffnesses increase monotonously with the roughness. The increasing stiffness indicates a higher dilatancy effect and interface resistance with roughness, which is in agreement with the works [22, 54].

The rotation stiffness of elastic interface can be derived as in [16]:

$$k_r = K_{11}(d/2)^2 \quad (34)$$

where d is the current interface length between two blocks in contact.

3.2. Constitutive matrices

Three hexagonal patterns (regular, hourglass, and asymmetric) are used to form different RVEs [40]. The generation of the hexagonal geometry can be seen in Section 2.4. For these three hexagonal patterns, three scales are considered with different side lengths: $s = 1.0$ ($l = 0.3660$), $s = 0.5$ ($l = 0.1830$), and $s = 0.25$ ($l = 0.0915$) where s represents the scale of the hexagonal pattern and l is the side length. All the used hexagonal RVEs are depicted in Fig. 4. In Fig. 4, the centroids of the particles and outward unit normal vectors at the interfaces are showed in order to compute the micropolar constitutive matrix through a homogenization procedure described in [16], where the adopted spring stiffness at the elastic joint interfaces is listed in Table 1. For comparison, the constitutive matrices for classical Cauchy model can be calculated from the micropolar constitutive matrices as follows:

$$\begin{aligned} \hat{A}_{1111} &= A_{1111} \\ \hat{A}_{1122} &= A_{1122} \\ \hat{A}_{2222} &= A_{2222} \\ \hat{A}_{1112} &= (A_{1112} + A_{1121})/2 \\ \hat{A}_{2212} &= (A_{2212} + A_{2221})/2 \\ \hat{A}_{1212} &= (A_{1212} + A_{2121} + 2A_{1221})/4 \end{aligned} \quad (35)$$

where the Cauchy constitutive components are characterized by the $\hat{\cdot}$ symbol. All micropolar and Cauchy constitutive matrices used in this paper are listed in Tables 2-7, of which components with all zeros are not reported. The superscripts (1.0) , (0.5) and (0.25) indicate the constitutive components when $s = 1.0, 0.5, 0.25$, respectively. When such specification is not present it means that the quantity does not change with the material scale.

3.3. Simulation results

A slope case was used to investigate the dilatancy effect with different contact density functions ($\Omega_1 \sim \Omega_5$). The slope is a right trapezoidal domain with height and top base of 9.6 m and bottom base equal to 19.2 m. Fig. 5 presents a sketch and finite element mesh (32×15) of the slope domain which is fixed at the bottom and symmetrically restrained at the right side. It is subjected to a top load acting on half of the top base of the slope with pressure $p = 10$ MPa.

Since the quadratic and linear interpolation functions have been assumed for the displacements and rotations respectively, the displacements are modeled with nine nodes and the microrotation is related to the four corner nodes. Three hexagonal patterns including regular, hourglass and asymmetric RVEs are used to perform simulations with different contact density functions. The simulation results are shown below.

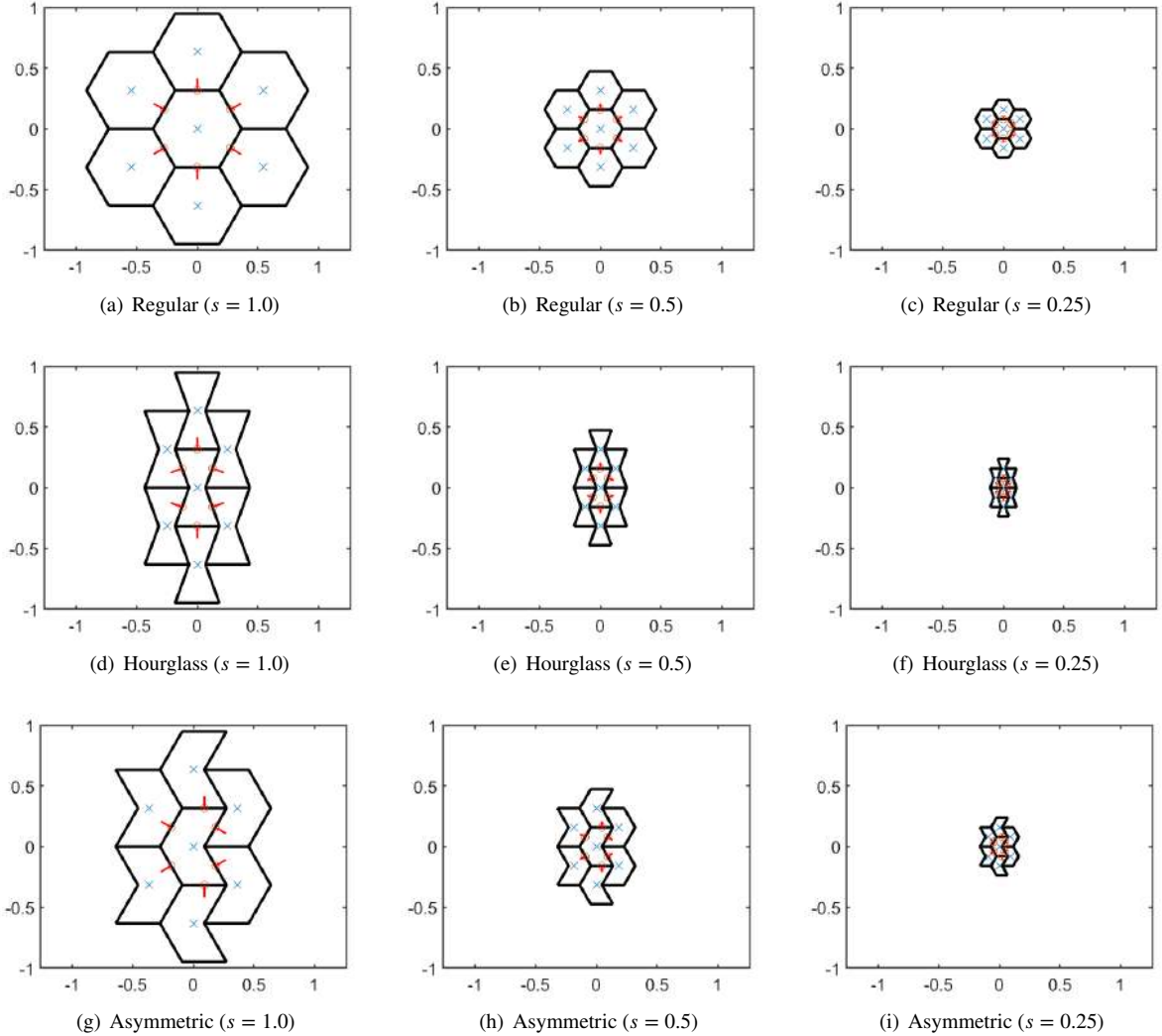


Figure 4: Hexagonal pattern RVE at different scales.

3.3.1. Regular

Table 2 lists the micropolar constitutive components for RVE assembled from the regular hexagonal particles. It can be seen that the values of A_{1112} , A_{1121} , A_{2212} and A_{2221} are non-zeros, meaning there is dilatancy effect. A_{1112} and A_{1121} relate horizontal stress and two tangential strains and A_{2212} and A_{2221} relate vertical stress and two tangential strains. It should be noted that A_{1112} and A_{1121} are opposite, which results in no dilatancy effect for Cauchy model ($\hat{A}_{1112} = 0$). The same phenomenon can be observed for A_{2212} and A_{2221} and their corresponding Cauchy constitutive component ($\hat{A}_{2212} = 0$), see Table 3. A Poisson effect occurs in this RVE, whereas there is no coupling between stresses/curvatures and microcouples/strains ($\mathbb{B} = 0$). The matrix \mathbb{A} remains unchanged with the scales, while matrix \mathbb{D} depends on the scales. The relationship between \mathbb{D} matrices from different scales is $\mathbb{D}^{(1.0)} \cong 4\mathbb{D}^{(0.5)} \cong 16\mathbb{D}^{(0.25)}$. D_{12} gives negligible values. The values of D_{11} and D_{22} are comparable for the regular RVE.

The simulation results of the regular case are shown in Figs. 6-11.

The vertical displacements u_2 (Fig. 6) concentrate in the area below the applied load. The micropolar model shows a comparable u_2 distribution with the Cauchy model. There is no evident difference among different scales for micropolar results. u_2 also shows no obvious changes as roughness increases for the two models.

The vertical stress σ_{22} (Fig. 7) shows a percolation [67] in both models. We can also observe that σ_{22} concentrated

Table 2
Micropolar constitutive components for regular RVE.

	Ω_1	Ω_2	Ω_3	Ω_4	Ω_5
A_{1111}	874.71	914.69	929.93	956.04	1006.6
A_{1122}	123.96	93.152	84.416	71.792	52.981
A_{1112}	-14.209	-79.384	-87.564	-96.715	-105.96
A_{1121}	14.209	79.384	87.564	96.715	105.96
A_{2222}	874.71	914.69	929.93	956.04	1006.6
A_{2212}	-14.209	-79.384	-87.564	-96.715	-105.96
A_{2221}	14.209	79.384	87.564	96.715	105.96
A_{1212}	626.79	728.38	761.10	812.46	900.67
A_{1221}	123.96	93.152	84.416	71.792	52.981
A_{2121}	626.79	728.38	761.10	812.46	900.67
$D_{11}^{(1,0)}$	79.822	94.465	99.141	106.44	118.89
$D_{12}^{(1,0)}$	-0.47592	-2.6588	-2.9328	-3.2393	-3.5490
$D_{22}^{(1,0)}$	65.291	83.545	89.245	98.028	112.68
$D_{11}^{(0,5)}$	19.956	23.616	24.785	26.611	29.723
$D_{12}^{(0,5)}$	-0.11898	-0.66471	-0.73321	-0.80983	-0.88726
$D_{22}^{(0,5)}$	16.323	20.886	22.311	24.507	28.170
$D_{11}^{(0,25)}$	4.9889	5.9041	6.1963	6.6527	7.4308
$D_{12}^{(0,25)}$	-0.029745	-0.16618	-0.18330	-0.20246	-0.22181
$D_{22}^{(0,25)}$	4.0807	5.2216	5.5778	6.1267	7.0426

Table 3
Cauchy constitutive components for regular RVE.

	Ω_1	Ω_2	Ω_3	Ω_4	Ω_5
\hat{A}_{1111}	874.71	914.69	929.93	956.04	1006.6
\hat{A}_{1122}	123.96	93.152	84.416	71.792	52.981
\hat{A}_{2222}	874.71	914.69	929.93	956.04	1006.6
\hat{A}_{1212}	375.38	410.77	422.76	442.13	476.83

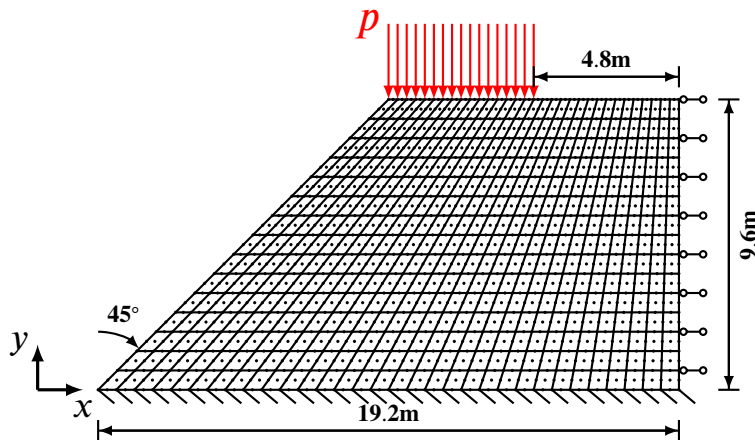


Figure 5: Sketch of the slope case with its finite element mesh.

under the applied load increases slightly as the scales decrease, meaning that there is a small scale effect on σ_{22} due to the change in matrix \mathbb{D} . As mentioned in [63], higher values of the \mathbb{D} components would result in a reduction of stress gradients. According to the roughness, it can be seen that there is no evident effect of roughness on σ_{22} for both

Table 4
Micropolar constitutive components for hourglass RVE.

	Ω_1	Ω_2	Ω_3	Ω_4	Ω_5
A_{1111}	429.44	440.21	445.05	453.90	472.43
A_{1122}	-92.006	-69.140	-62.656	-53.286	-39.324
A_{1112}	10.546	58.921	64.993	71.784	78.648
A_{1121}	9.9385	55.524	61.246	67.646	74.114
A_{2222}	1867.8	1967.4	2004.2	2066.3	2184.4
A_{2212}	-25.604	-143.04	-157.79	-174.27	-190.94
A_{2221}	-10.546	-58.921	-64.993	-71.784	-78.648
A_{1212}	1421.1	1631.7	1699.9	1807.5	1993.5
A_{1221}	-92.006	-69.140	-62.656	-53.286	-39.324
A_{2121}	256.04	309.90	326.96	353.47	398.31
$D_{11}^{(1,0)}$	29.916	30.621	30.944	31.540	32.798
$D_{12}^{(1,0)}$	-0.10001	-0.55872	-0.61630	-0.68071	-0.74579
$D_{22}^{(1,0)}$	145.36	172.60	181.29	194.85	217.93
$D_{11}^{(0,5)}$	7.4790	7.6551	7.7360	7.8851	8.1996
$D_{12}^{(0,5)}$	-0.025002	-0.13968	-0.15408	-0.17018	-0.18645
$D_{22}^{(0,5)}$	36.339	43.150	45.322	48.712	54.483
$D_{11}^{(0,25)}$	1.8698	1.9138	1.9340	1.9713	2.0499
$D_{12}^{(0,25)}$	-0.0062505	-0.034920	-0.038519	-0.042544	-0.046612
$D_{22}^{(0,25)}$	9.0847	10.788	11.331	12.178	13.621

Table 5
Cauchy constitutive components for hourglass RVE.

	Ω_1	Ω_2	Ω_3	Ω_4	Ω_5
\hat{A}_{1111}	429.44	440.21	445.05	453.90	472.43
\hat{A}_{1122}	-92.006	-69.140	-62.656	-53.286	-39.324
\hat{A}_{1112}	10.242	57.222	63.120	69.715	76.381
\hat{A}_{2222}	1867.8	1967.4	2004.2	2066.3	2184.4
\hat{A}_{2212}	-18.075	-100.98	-111.39	-123.03	-134.79
\hat{A}_{1212}	373.28	450.83	475.39	513.60	578.29

micropolar and Cauchy models.

The relative rotation $\vartheta - \omega$ for the micropolar model is depicted in Fig. 8. $\vartheta - \omega$ can be mainly observed in the area near the applied load. The values of $\vartheta - \omega$ are small and close to zero for all configurations, indicating a very small micropolar effect in the case of regular RVE, as discussed by the authors in [44].

Figs. 9 and 10 show the tangential strains of both models. As mentioned above, for the micropolar model $\varepsilon_{12} \neq \varepsilon_{21}$, whereas these two values are equal for the Cauchy model. Thus, the figures for the Cauchy model in Figs. 9 and 10 are the same. The contour plots show a pair of opposite tangential strains concentrated below the two sides of the applied load and spread towards the boundary. There can be seen a scale effect for both two tangential strains in the case of the micropolar model, the magnitudes of tangential strains (whether positive or negative) increase as the scale decreases. For the micropolar model, these two tangential strains show different trends with the change of roughness. For ε_{12} , the positive tangential strain in the right side of the slope decreases with respect to roughness, while the negative tangential strain in the left side does not change obviously. On the contrary, for ε_{21} , the negative tangential strain in the left side recedes with roughness and the positive tangential strain in the right side has no obvious change. The Cauchy model shows that the magnitudes of tangential strains on both sides decrease with roughness, but such a decrease is less evident than that in the micropolar model. This is because there is no dilatancy effect in the Cauchy model for the regular RVE. The decrease in strain with roughness can be attributed to the variation of other constitutive components. It can also be seen that two tangential strains of the micropolar model show a close behavior to that of the Cauchy model, especially for the smooth interface (Ω_1), which reveals that the regular RVE has a similar behavior

Table 6
Micropolar constitutive components for asymmetric RVE.

	Ω_1	Ω_2	Ω_3	Ω_4	Ω_5
A_{1111}	583.14	609.79	619.96	637.36	671.09
A_{1121}	9.4728	52.922	58.376	64.476	70.641
A_{2222}	1312.1	1372.0	1394.9	1434.1	1510.0
A_{2212}	-21.314	-119.08	-131.35	-145.07	-158.94
A_{1212}	940.19	1092.6	1141.7	1218.7	1351.0
A_{2121}	417.86	485.59	507.40	541.64	600.45
$B_{111}^{(1.0)}$	2.6005	14.528	16.025	17.700	19.392
$B_{221}^{(1.0)}$	2.6005	14.528	16.025	17.700	19.392
$B_{222}^{(1.0)}$	91.385	92.224	92.819	94.053	96.962
$B_{122}^{(1.0)}$	1.9503	10.896	12.019	13.275	14.544
$B_{212}^{(1.0)}$	2.6005	14.528	16.025	17.700	19.392
$B_{111}^{(0.5)}$	1.3002	7.2641	8.0127	8.8500	9.6962
$B_{221}^{(0.5)}$	1.3002	7.2641	8.0127	8.8500	9.6962
$B_{222}^{(0.5)}$	45.692	46.112	46.410	47.027	48.481
$B_{122}^{(0.5)}$	0.97517	5.4481	6.0095	6.6375	7.2721
$B_{212}^{(0.5)}$	1.3002	7.2641	8.0127	8.8500	9.6962
$B_{111}^{(0.25)}$	0.65011	3.6320	4.0063	4.4250	4.8481
$B_{221}^{(0.25)}$	0.65011	3.6320	4.0063	4.4250	4.8481
$B_{222}^{(0.25)}$	22.846	23.056	23.205	23.513	24.240
$B_{122}^{(0.25)}$	0.48758	2.7240	3.0048	3.3188	3.6361
$B_{212}^{(0.25)}$	0.65011	3.6320	4.0063	4.4250	4.8481
$D_{11}^{(1.0)}$	48.176	52.006	53.333	55.500	59.446
$D_{12}^{(1.0)}$	-0.47592	-2.6588	-2.9328	-3.2393	-3.5490
$D_{22}^{(1.0)}$	111.86	132.55	139.15	149.46	167.03
$D_{11}^{(0.5)}$	12.044	13.002	13.333	13.875	14.862
$D_{12}^{(0.5)}$	-0.11898	-0.66471	-0.73321	-0.80983	-0.88726
$D_{22}^{(0.5)}$	27.965	33.137	34.788	37.365	41.757
$D_{11}^{(0.25)}$	3.0110	3.2504	3.3333	3.4687	3.7154
$D_{12}^{(0.25)}$	-0.029745	-0.16618	-0.18330	-0.20246	-0.22181
$D_{22}^{(0.25)}$	6.9913	8.2843	8.6970	9.3413	10.439

Table 7
Cauchy constitutive components for asymmetric RVE.

	Ω_1	Ω_2	Ω_3	Ω_4	Ω_5
\hat{A}_{1111}	583.14	609.79	619.96	637.36	671.09
\hat{A}_{1112}	4.7364	26.461	29.188	32.238	35.321
\hat{A}_{2222}	1312.1	1372.0	1394.9	1434.1	1510.0
\hat{A}_{2212}	-10.657	-59.540	-65.675	-72.535	-79.470
\hat{A}_{1212}	339.51	394.55	412.27	440.09	487.86

to the classical continuum. As the dilatancy effect increases in micropolar model, the difference in tangential strains between two models becomes more evident with increasing roughness.

Micropolar microrotation ω and Cauchy macrorotation ϑ are comparable as shown in Fig. 11. There is no obvious difference between these two measures, i.e. $\vartheta \approx \omega$, resulting in very small relative rotations as shown in 8, however Fig. 11 displays the gradient of such quantity which is not represented by the relative rotation in Fig. 8. The distributions of these two rotations in the slope domain are similar to tangential strains. A pair of opposite rotations is mainly distributed below the two sides of the applied load and diffuse away from the load. The positive ω and ϑ below the right side of the applied load show a slight decrease as the roughness increases. However, there is no obvious scale

The effects of dilatancy in composite assemblies as micropolar continua

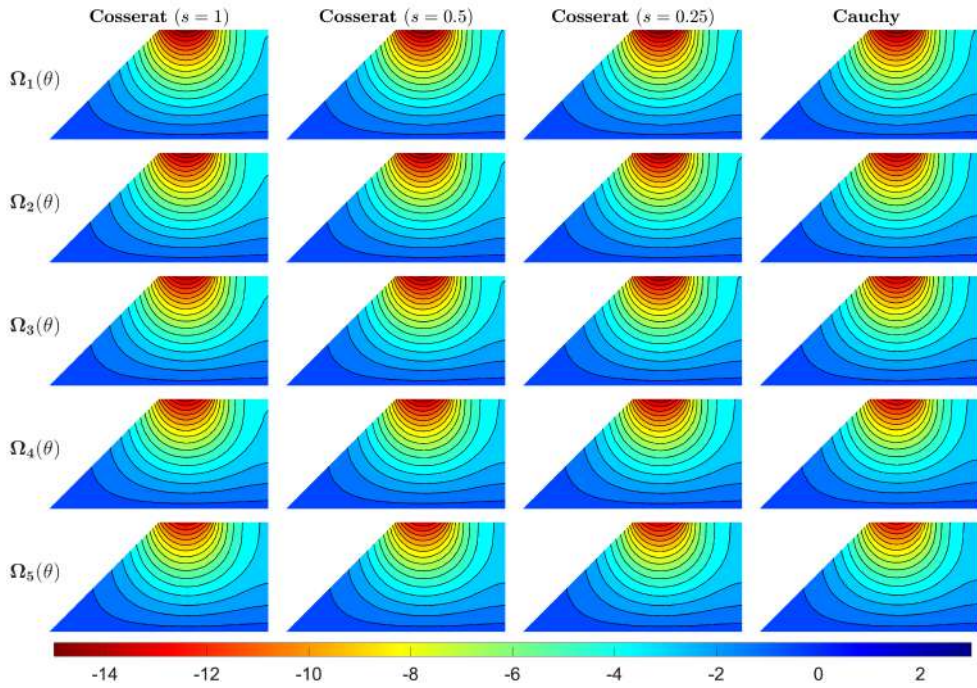


Figure 6: Vertical displacement u_2 for regular RVE.

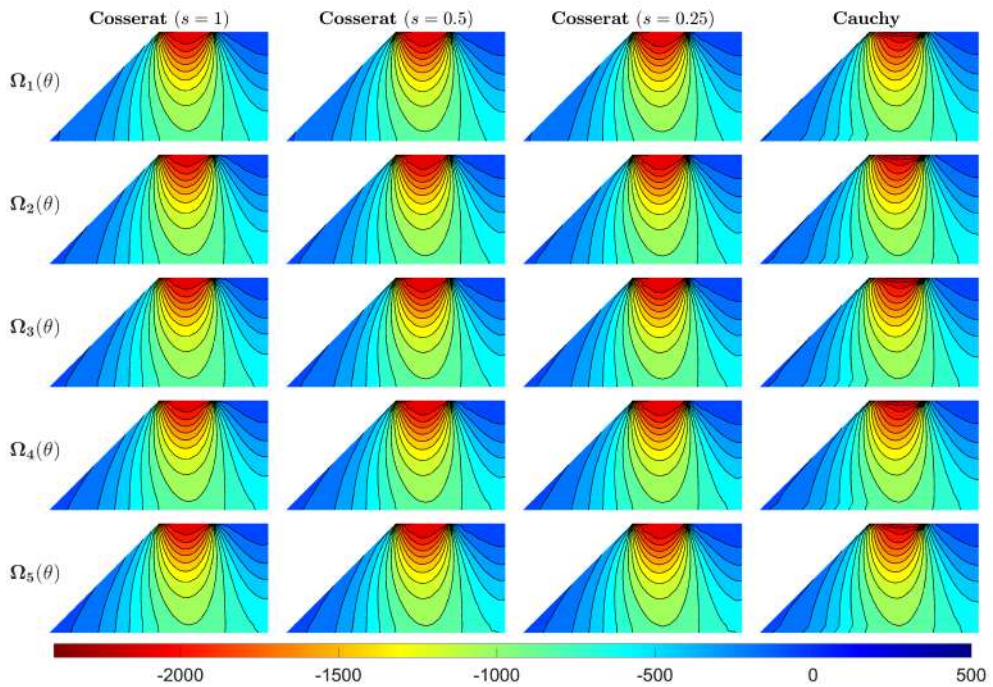


Figure 7: Vertical stress σ_{22} for regular RVE.

effect on ω for the micropolar model.

The effects of dilatancy in composite assemblies as micropolar continua

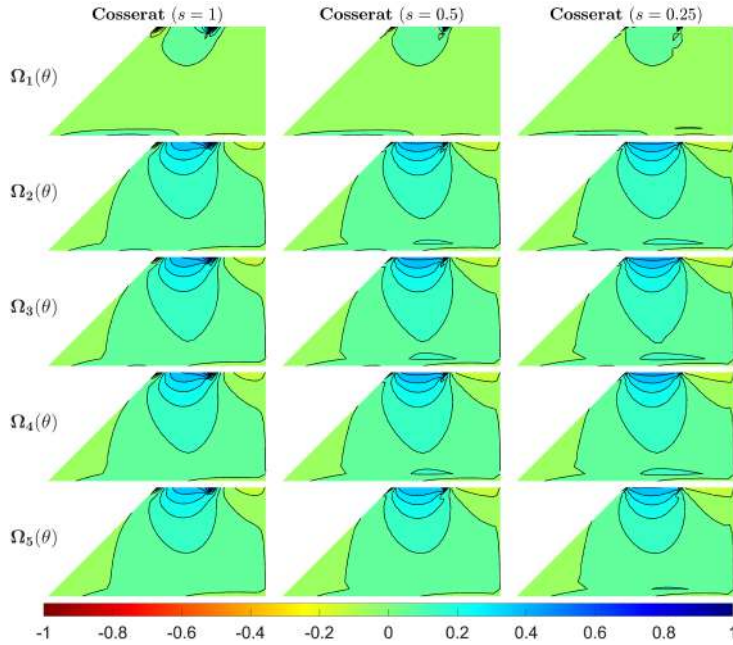


Figure 8: Cosserat relative rotation $\vartheta - \omega$ for regular RVE.

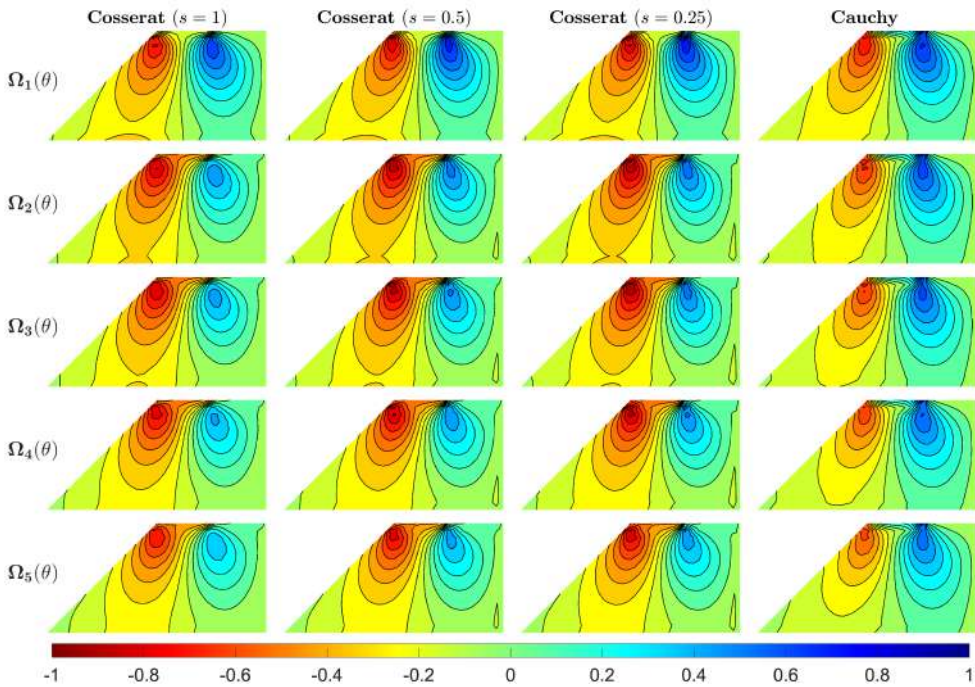


Figure 9: Tangential strain ϵ_{12} for regular RVE.

3.3.2. Hourglass

Table 4 lists the micropolar constitutive components for the hourglass RVE. Similarly to regular RVE, there is no coupling between stresses/curvatures and microcouples/strains ($\mathbb{B} = 0$). An auxetic (negative Poisson effect) nature is observed. The dilatancy components (A_{1112} , A_{1121} , A_{2212} and A_{2221}) are non-zeros, meaning there is dilatancy effect.

The effects of dilatancy in composite assemblies as micropolar continua

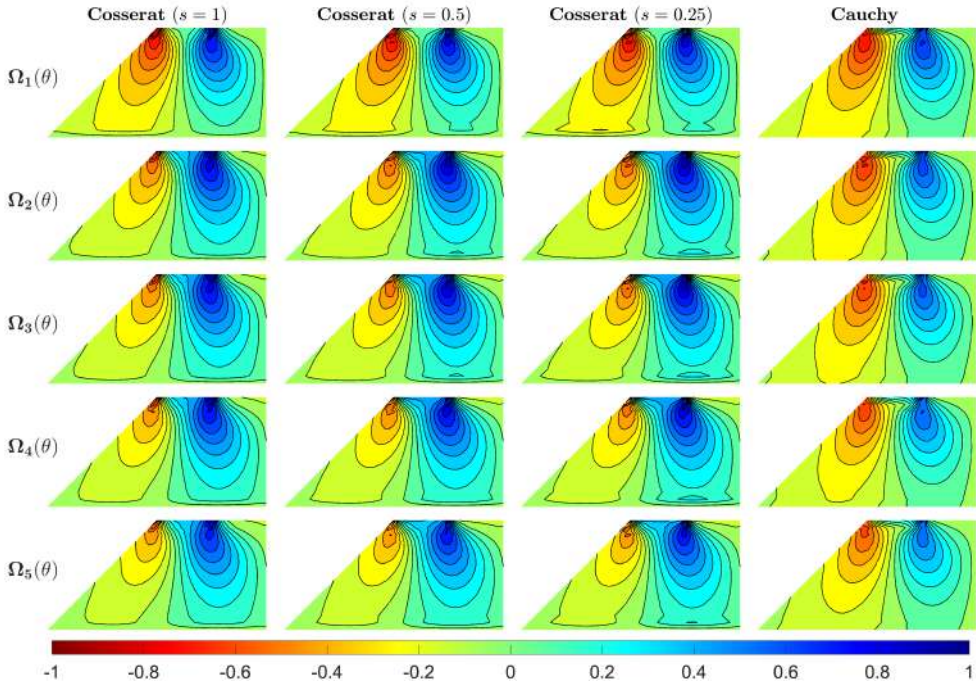


Figure 10: Tangential strain ε_{21} for regular RVE.

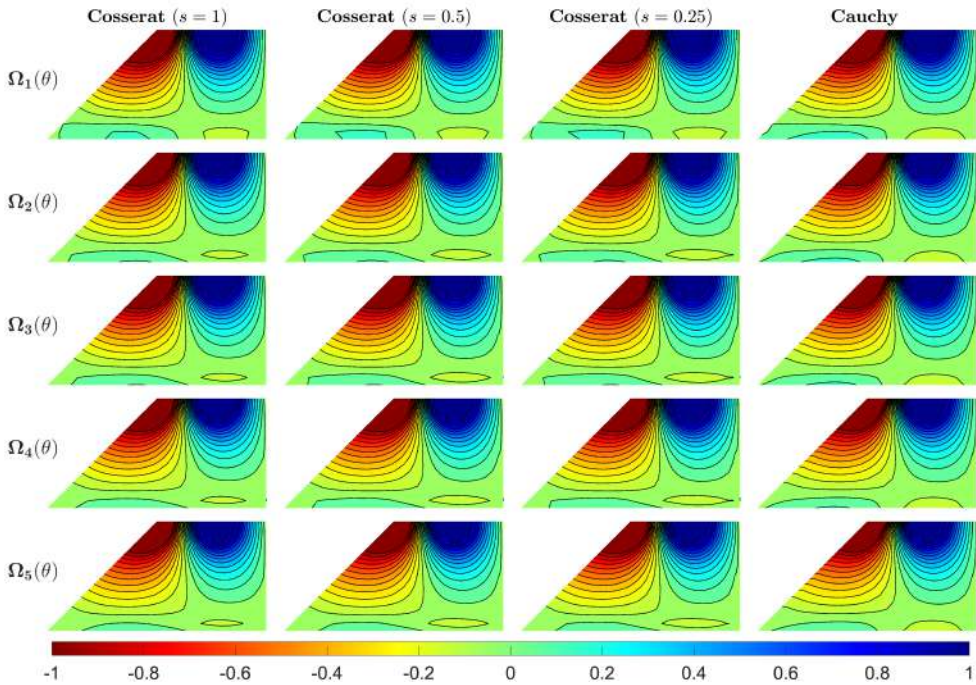


Figure 11: Cosserat microrotation ω and Cauchy macrorotation ϑ for regular RVE.

Here, $A_{1112} \neq A_{1121}$ and $A_{2212} \neq A_{2221}$, which result in dilatancy effect in Cauchy model (\hat{A}_{1112} and \hat{A}_{2212} are not equal to 0) in Table 5. It is noted that only matrix \mathbb{D} depends on the scale and the ratio of \mathbb{D} among three scales is the same as in the previous cases ($\mathbb{D}^{(1.0)} \cong 4\mathbb{D}^{(0.5)} \cong 16\mathbb{D}^{(0.25)}$). D_{12} also gives negligible values, whereas D_{11} is smaller

than D_{22} .

The simulation results are depicted in Figs. 12-17. u_2 (Figs. 12), has comparable behavior with respect to the correspondent regular cases but they have smaller intensity. The concentrated u_2 is close to zero far from the applied load, showing the effect of the negative Poisson ratio in the hourglass case. Moreover, u_2 shows a slight decrease trend with the increasing roughness for both two models.

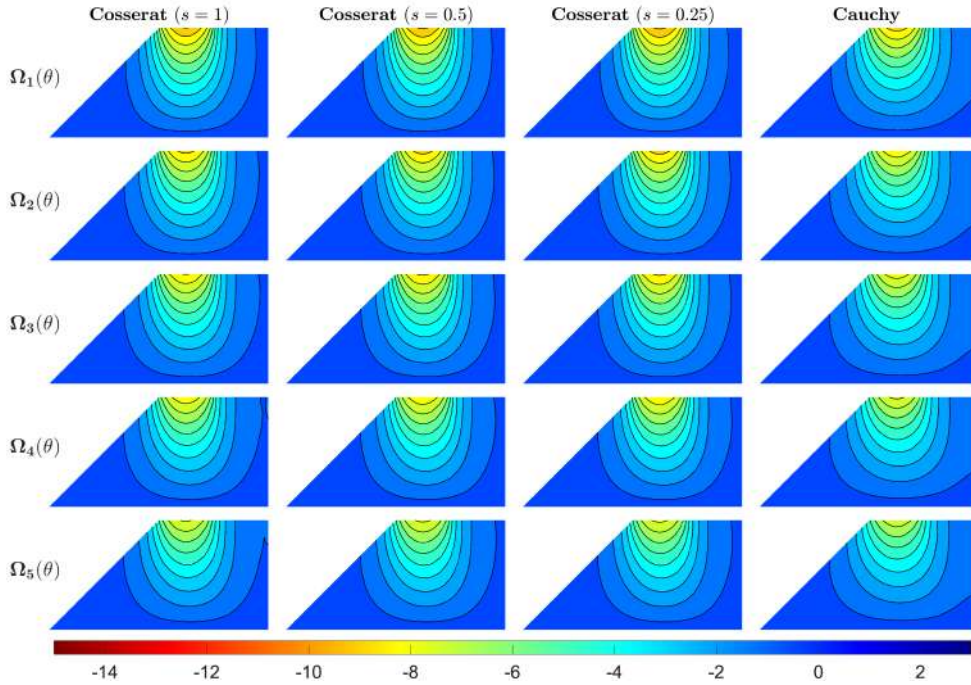


Figure 12: Vertical displacement u_2 for hourglass RVE.

σ_{22} (Fig. 13) shows better percolation and higher stress value than the ones of the correspondent regular case in Fig. 7. The vertical stress percolation reduces with the increase in roughness for both models. For the micropolar model, the concentrated σ_{22} increases slightly with the decrease in scale due to the small \mathbb{D} values for small scale cases.

Relative rotation, $\vartheta - \omega$, shows a clear micropolar effect in the hourglass case. A pair of opposite relative rotations are concentrated below the two sides of the applied load. $\vartheta - \omega$ below the left side of load shows negative values of relative rotation, whereas $\vartheta - \omega$ below the right side shows positive values. It can be seen that the value of $\vartheta - \omega$ trends to increase as scale decreases. The micropolar effect decreases as the roughness increases, which means that such a micropolar effect is stronger for smoother interfaces. This result is in line with Brahimian et al. [51] who also found a higher microrotation in the smooth boundaries of granular Cosserat materials.

The tangential strain ε_{12} (Fig. 15) is smaller than that in regular RVE, whereas ε_{21} (Fig. 16) shows much higher values than for regular RVE. The tangential strain of the Cauchy model is not close to the two tangential strains of the micropolar model but lies in the middle of them. For the micropolar model, the magnitudes of ε_{12} and ε_{21} both increase with a decrease in scale. For both models, the tangential strain decreases as roughness increases.

Micropolar microrotation ω and Cauchy macrorotation ϑ (Fig. 17) show similar distribution as the regular case. However, the difference between these two rotations becomes more obvious than for the regular RVE, indicating a more obvious micropolar effect for the hourglass RVE. For both models, these two rotations show a decreasing trend as roughness increases. For the micropolar model, the magnitude of ω has no evident scale effect. For both models, ω and ϑ decreases as the roughness increases.

A reduction trend with roughness can be found here especially for measurements like rotation (including microrotation, macrorotation, and relative rotation) and tangential strains. This can be attributed to the increasing interlocking and dilatancy effect with roughness as mentioned above. The magnitudes of dilatancy constitutive components increasing with roughness (Tables. 2-7), indicating a higher degree of interlocking for the rougher interface. With

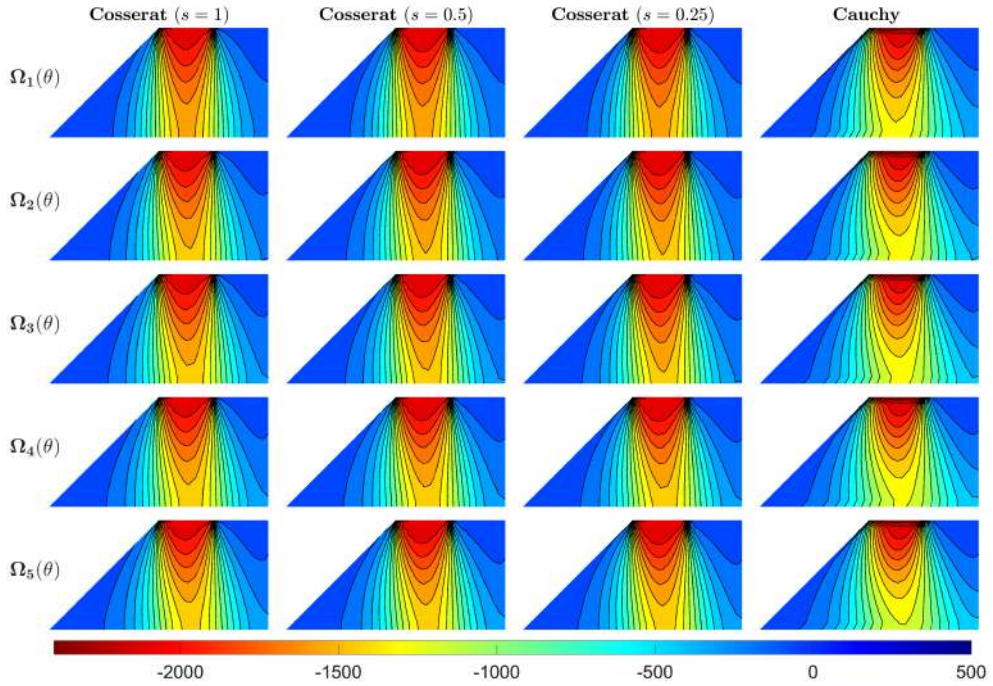


Figure 13: Vertical stress σ_{22} for hourglass RVE.

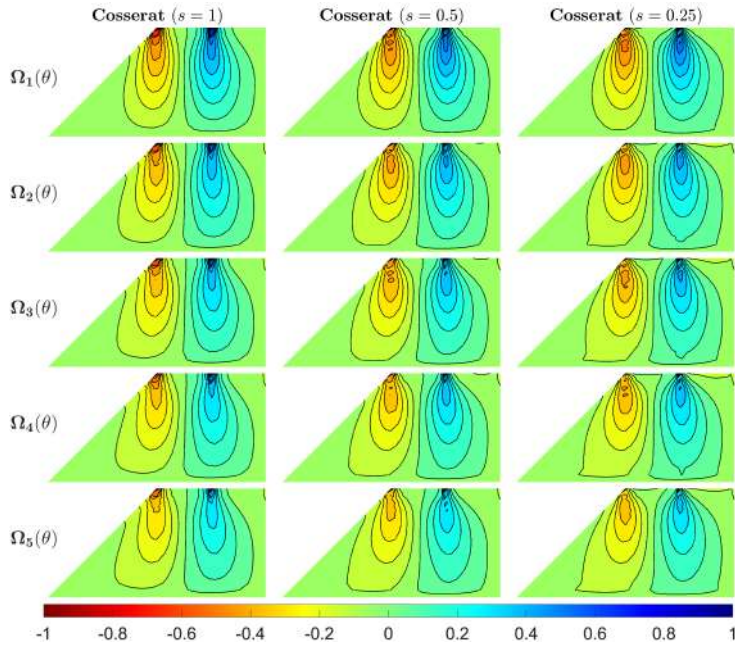


Figure 14: Cosserat relative rotation $\theta - \omega$ for hourglass RVE.

higher interlocking, rougher interfaces are more resistant to against deformation [22, 68, 69]. Therefore, the measurements decrease as interface roughness increases. Such phenomenon can be also observed in the cases of regular and asymmetric RVEs.

The effects of dilatancy in composite assemblies as micropolar continua

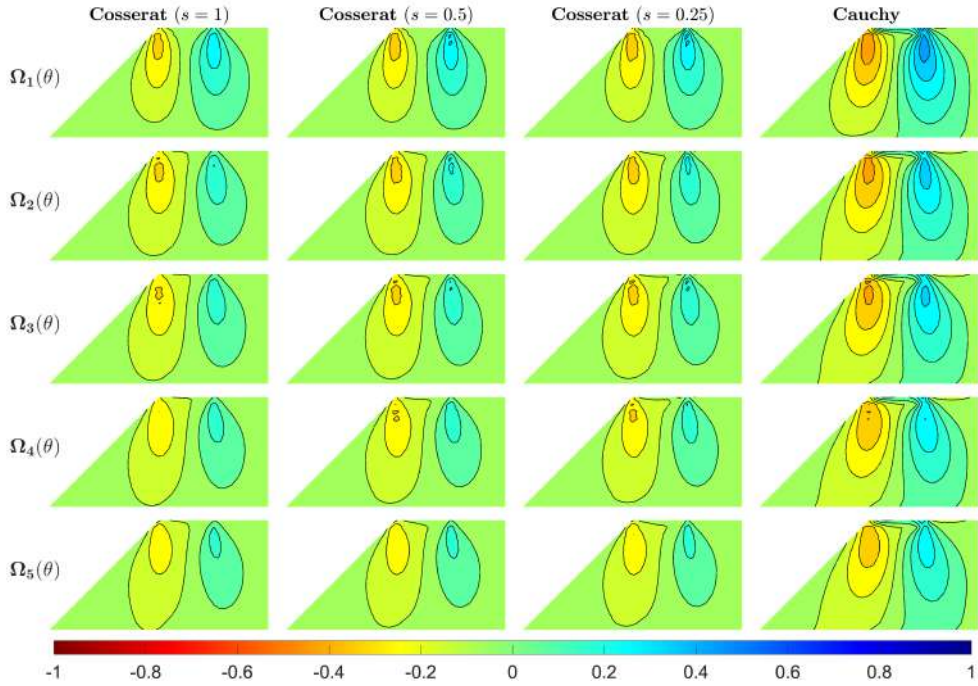


Figure 15: Tangential strain ε_{12} for hourglass RVE.

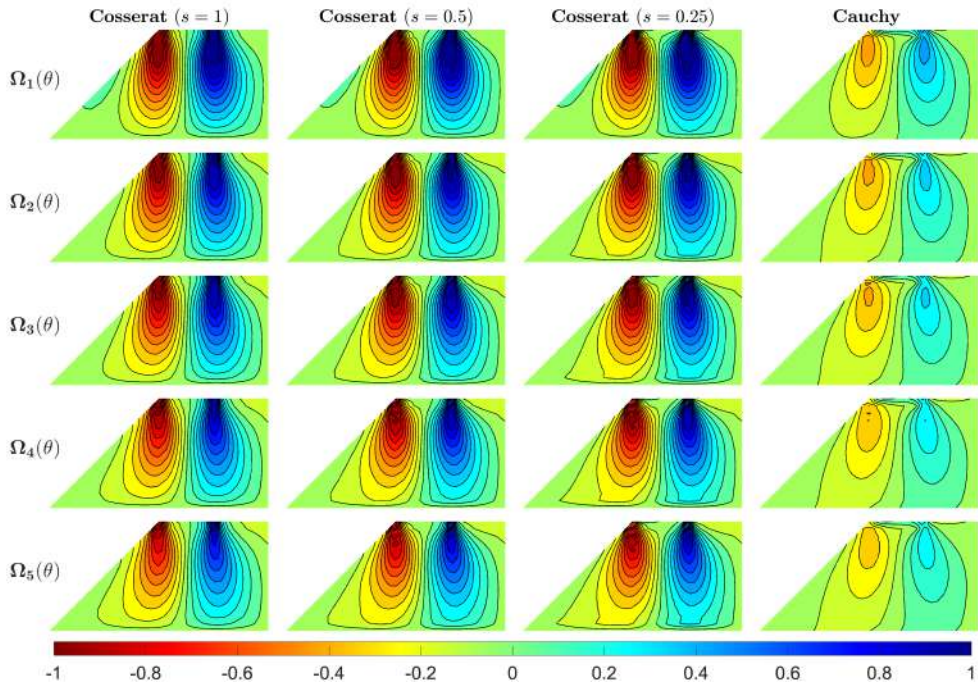


Figure 16: Tangential strain ε_{21} for hourglass RVE.

3.3.3. Asymmetric

Tables 6 and 7 list the constitutive components for the asymmetric RVE. It can be seen that there is less non-zero components of matrix \mathbb{A} . No Poisson effect is observed, while the dilatancy effect still exist for both micropolar and

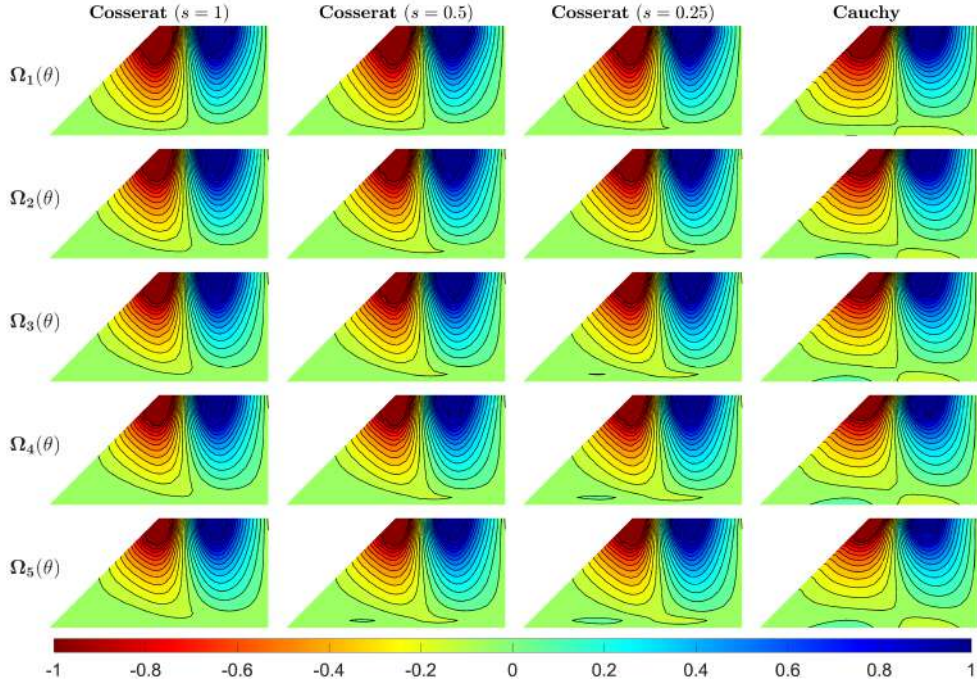


Figure 17: Cosserat microrotation ω and Cauchy macrorotation ϑ for hourglass RVE.

Cauchy models. The matrix $\mathbb{B} \neq 0$, meaning a coupling between stresses/curvatures and microcouples/strains occurs. \mathbb{B} and \mathbb{D} depend on the scale. The ratio of \mathbb{B} among three scales is $\mathbb{B}^{(1.0)} \cong 2\mathbb{B}^{(0.5)} \cong 4\mathbb{B}^{(0.25)}$ and the ratio of \mathbb{D} is the same as previous ones ($\mathbb{D}^{(1.0)} \cong 4\mathbb{D}^{(0.5)} \cong 16\mathbb{D}^{(0.25)}$). The values of D_{11} are smaller than that of D_{22} and the values of D_{12} are negligible again.

Figs. 18-23 present the simulation results for the asymmetric RVE. All measurements of this case have similar behavior with the correspondent hourglass case but with different intensities. u_2 (Fig. 18) is larger than the hourglass RVE but smaller than the regular case. The level of σ_{22} (Fig. 19) percolation is lower than that of the hourglass case but higher than that of the regular case. The magnitude of stress percolation can be related to the anisotropy degree of material [67, 70]. The most evident percolation is shown in the hourglass case as the higher degree of anisotropy, whereas the regular case has the lowest percolation as this case behaves like an isotropic material as described already in [40]. The relative rotation $\vartheta - \omega$ (Fig. 20) is less evident than in the case of the hourglass because of the introduction of the non-zero matrix \mathbb{B} . The tangential strain ε_{12} (Fig. 21) is greater than that in hourglass results but smaller than in regular results; on the contrary, ε_{21} (Fig. 22) show much smaller values than that in hourglass results but greater than in regular results.

4. Conclusions

This work presents the mechanical behavior of composite materials with hexagonal microstructures described as equivalent micropolar continuum. In particular, the dilatancy effect is investigated by changing interface roughness of the microstructure. Dilatancy stiffness computed by the contact density model increases with the interface roughness. Three hexagonal geometries termed regular, hourglass, and asymmetric are selected and each one of them shows some peculiar characteristics. The size effect of the microstructure is investigated by considering three internal length scales that affects the scale-dependent micropolar constitutive constants. For comparison, the results of classical Cauchy model is also presented here.

For three different hexagonal geometries, the regular one shows a behavior similar to the classical continuum, therefore it has weaker dependence on the dilatancy and scale effects compared with the other two geometries. The hexagonal geometries with different anisotropic degrees influence the percolation of load. An increasing degree of anisotropy corresponds to a significant percolation of stress. The hourglass hexagon shows the greatest percolation of

The effects of dilatancy in composite assemblies as micropolar continua

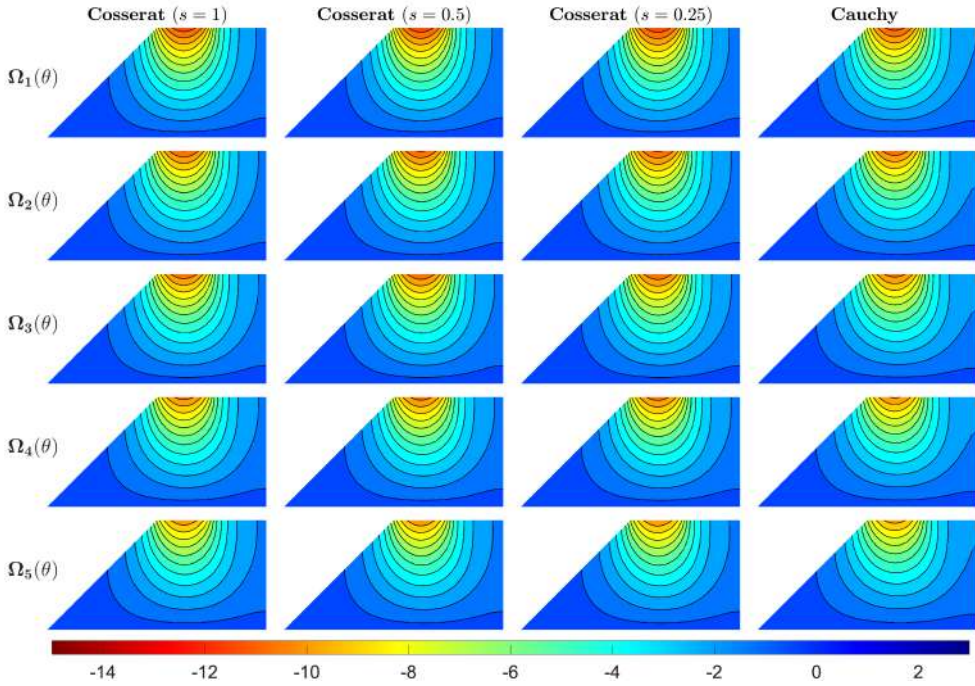


Figure 18: Vertical displacement u_2 for asymmetric RVE.

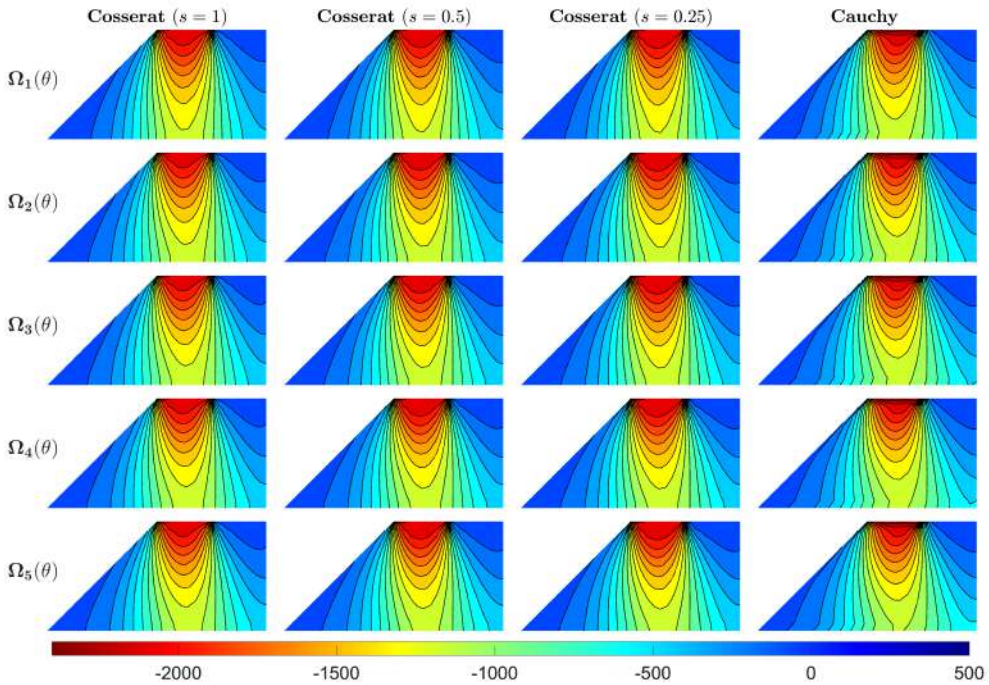


Figure 19: Vertical stress σ_{22} for asymmetric RVE.

vertical stress in the slope panel, followed by asymmetric and regular patterns. There is no significant effect of dilatancy on the displacements and stresses. For the rotations (including the relative rotation and microrotation for the micropolar model and macrorotation for the Cauchy model) and non-symmetric tangential strains, the effect of dilatancy is more

The effects of dilatancy in composite assemblies as micropolar continua

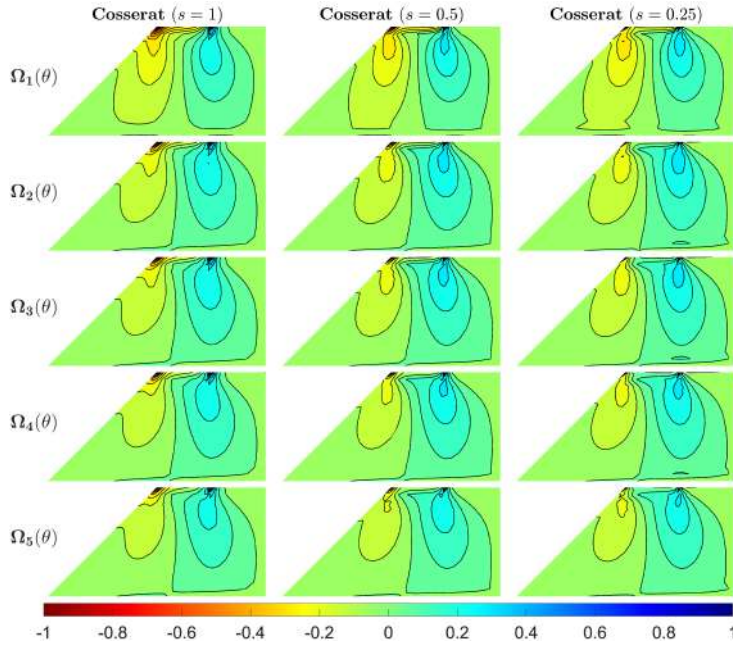


Figure 20: Cosserat relative rotation $\theta - \omega$ for asymmetric RVE.

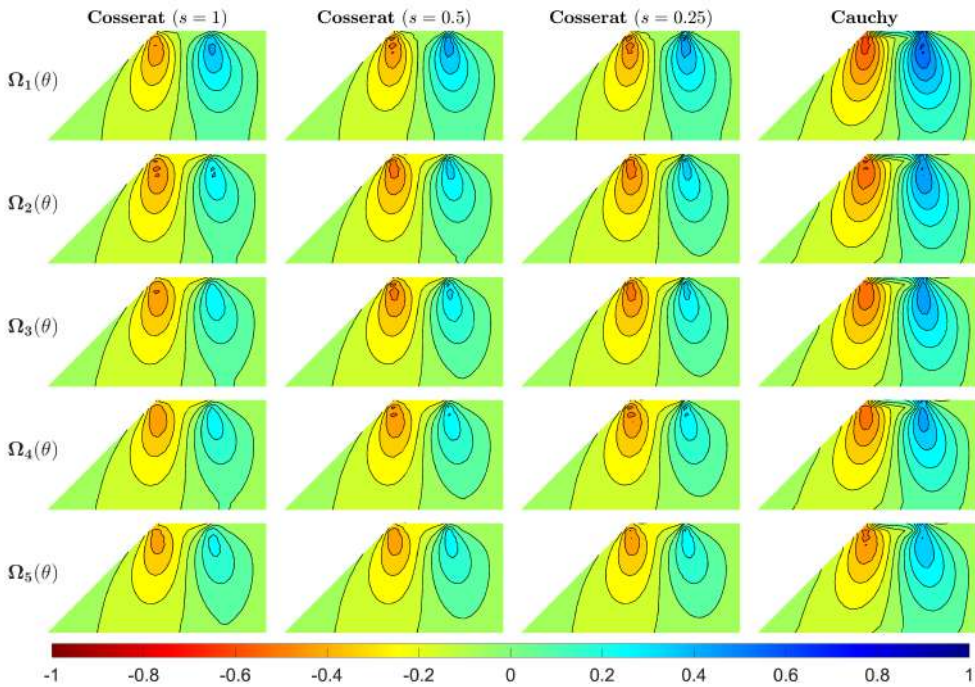


Figure 21: Tangential strain ε_{12} for asymmetric RVE.

evident. In general, the magnitudes of these measurements decrease with the roughness, indicating that the increasing dilatancy effect can alleviate rotation distribution as well as the micropolar effect. This is because rougher interface is more interlocked and can provide higher interface resistance compared to smooth interfaces. Moreover, the percolation of stress also decreases with the increasing roughness, meaning that the increase in dilatancy can suppress the diffusion

The effects of dilatancy in composite assemblies as micropolar continua

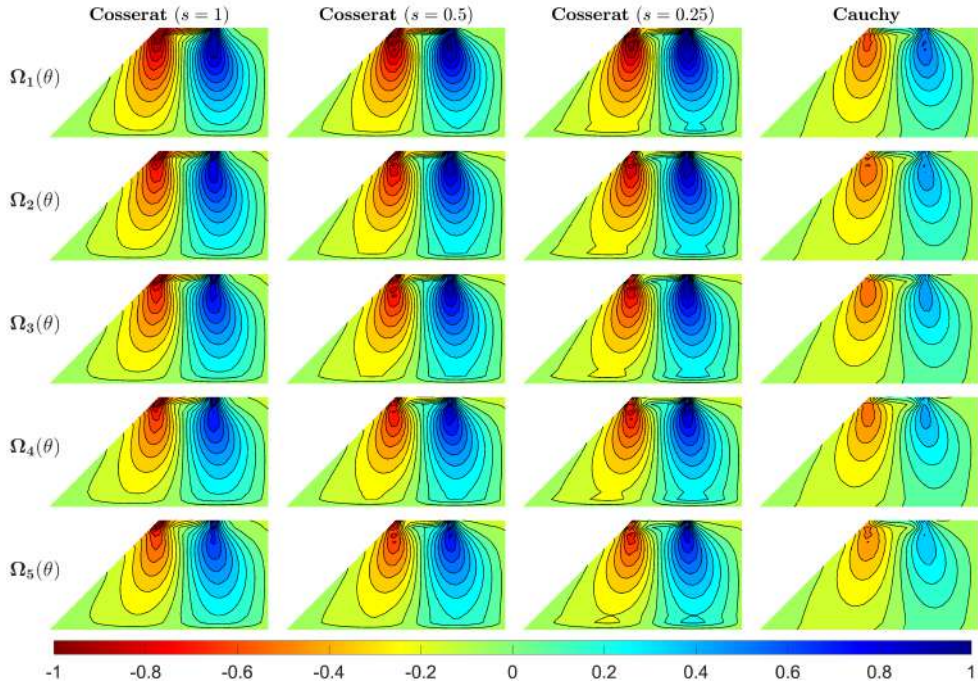


Figure 22: Tangential strain ε_{21} for asymmetric RVE.

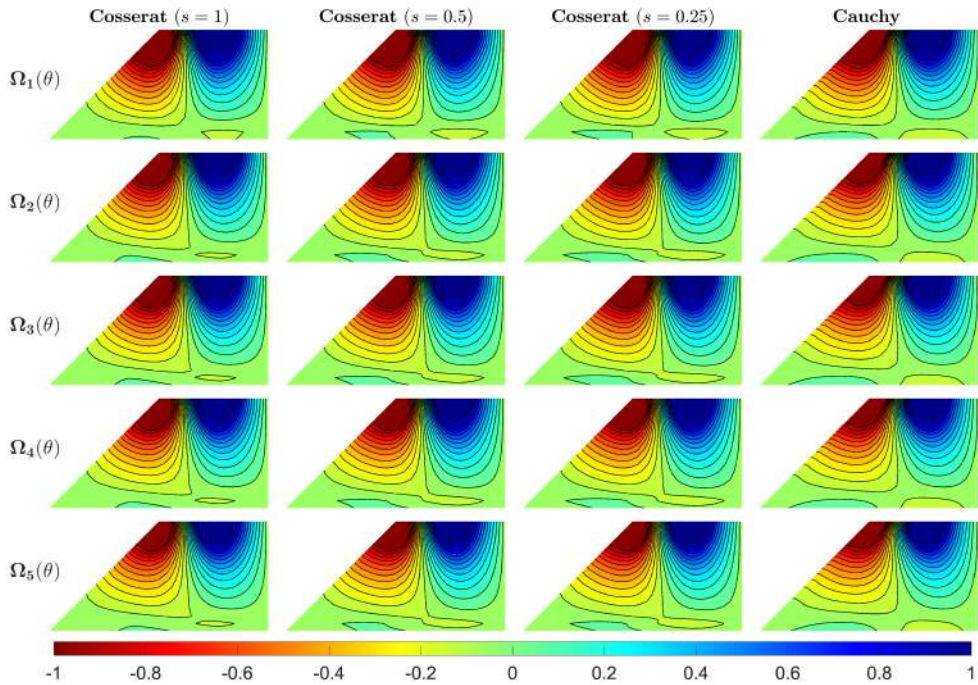


Figure 23: Cosserat microrotation ω and Cauchy macrorotation ϑ for asymmetric RVE.

of stress.

The scale effect is more evident for the measurements of vertical stress, relative rotation, and tangential strains. An increase in the scale of microstructure can alleviate these results, i.e. bring smaller relative rotation, stress, and

tangential strains as scale increases. This aspect could be underlined due to the introduction of micropolar model. With the extra rotation degree of freedom compared with the Cauchy model, the micropolar continuum is able to investigate the relative rotation, non-symmetric stresses/strains, and their scale effect. This paper shows a clear dilatancy effect on the micropolar continuum with hourglass and asymmetric microstructures. The effect of dilatancy on other mechanical problems such as layered rock with rough joints is expected to be investigated in future studies.

Acknowledgements

The first author acknowledges the China Scholarship Council (CSC) for providing funds (No. 202006050138) to support his study and research at the University of Bologna.

This research was supported by the Italian Ministry of University and Research P.R.I.N. 2017 no. 20172017HFP-KZY (cup: B86J16002300001) and Sapienza Research Grants "Progetti Grandi" 2018 (B81G19000060005).

CRedit authorship contribution statement

Farui Shi: Methodology, Software, Validation, Formal analysis, Investigation, Data curation, Writing - Original draft preparation, Writing - Review & Editing. **Nicholas Fantuzzi:** Conceptualization of this study, Methodology, Software, Resources, Writing - Original draft preparation, Writing - Review & Editing, Supervision, Project administration. **Patrizia Trovalusci:** Conceptualization of this study, Methodology, Software, Resources, Writing - Review & Editing, Supervision, Project administration. **Yong Li:** Writing - Review & Editing, Visualization, Funding acquisition. **Zuoan Wei:** Resources, Writing - Review & Editing, Supervision.

Data Availability Statement

Some or all data, models, or code that support the findings of this study are available from the corresponding author upon reasonable request.

References

- [1] Max Tirassa, Miguel Fernández Ruiz, and Aurelio Muttoni. Influence of cracking and rough surface properties on the transfer of forces in cracked concrete. *Engineering Structures*, 225:111138, 2020.
- [2] Richard E Goodman. *Introduction to rock mechanics*, volume 2. Wiley New York, 1989.
- [3] M.M. Mehrabadi and S. Nemat-Nasser. Stress, dilatancy and fabric in granular materials. *Mechanics of Materials*, 2(2):155–161, 1983.
- [4] Antonio DeSimone and Claudio Tamagnini. Stress–dilatancy based modelling of granular materials and extensions to soils with crushable grains. *International Journal for Numerical and Analytical Methods in Geomechanics*, 29(1):73–101, 2005.
- [5] Xihua Chu, Cun Yu, and Yuanjie Xu. The dilatancy and numerical simulation of failure behavior of granular materials based on cosserat model. *Interaction and multiscale mechanics*, 5(2):157–168, 2012.
- [6] M.A. Kwafniewski and J.A. Wang. Surface roughness evolution and mechanical behavior of rock joints under shear. *International Journal of Rock Mechanics and Mining Sciences*, 34(3):157.e1–157.e14, 1997.
- [7] K. W. Cao, N. M. Khan, W. Liu, S. Hussain, Y. G. Zhu, Z. T. Cao, and Y. C. Bian. Prediction model of dilatancy stress based on brittle rock: A case study of sandstone. *Arabian Journal for Science and Engineering*, 46(3):2165–2176, 2021.
- [8] Masoud Shadlou, Ehsan Ahmadi, and Mohammad Mehdi Kashani. Micromechanical modelling of mortar joints and brick-mortar interfaces in masonry structures: A review of recent developments. *Structures*, 23:831–844, 2020.
- [9] Trovalusci, P. and Augusti, G. A continuum model with microstructure for materials with flaws and inclusions. *J. Phys. IV France*, 08:Pr8–383–Pr8–390, 1998.
- [10] M. Wallner, K.-H. Lux, W. Minkley, and Jr. H. Reginald Hardy. *The Mechanical Behavior of Salt – Understanding of THMC Processes in Salt: Proceedings of the 6th Conference (SaltMech6), Hannover, Germany, 22–25 May 2007 (1st ed.)*. CRC Press, 2007.
- [11] Daniele Baraldi, Emanuele Reccia, and Antonella Cecchi. In plane loaded masonry walls: Dem and fem/dem models. a critical review. *Meccanica*, 53(7):1613–1628, 2018.
- [12] Emanuele Reccia, L. Leonetti, Patrizia Trovalusci, and Antonella Cecchi. A multiscale/multidomain model for the failure analysis of masonry walls: A validation with a combined fem/dem approach. *International Journal for Multiscale Computational Engineering*, 16(4):325–343, 2018.
- [13] Holm Altenbach and Tomasz Sadowski. *Failure and damage analysis of advanced materials*. Springer, 2015.
- [14] Fabrizio Greco, Lorenzo Leonetti, Raimondo Luciano, and Paolo Nevone Blasi. Effects of microfracture and contact induced instabilities on the macroscopic response of finitely deformed elastic composites. *Composites Part B: Engineering*, 107:233–253, 2016.
- [15] Patrizia Trovalusci and Martin Ostoja-Starzewski. Multiscale mechanical modelling of complex materials and engineering applications 2. *International Journal for Multiscale Computational Engineering*, 9(5), 2011.
- [16] P. Trovalusci and R. Masiani. Material symmetries of micropolar continua equivalent to lattices. *International Journal of Solids and Structures*, 36(14):2091–2108, 1999.

- [17] Patrizia Trovalusci and Renato Masiani. Non-linear micropolar and classical continua for anisotropic discontinuous materials. *International Journal of Solids and Structures*, 40(5):1281–1297, 2003.
- [18] Patrizia Trovalusci and Annamaria Pau. Derivation of microstructured continua from lattice systems via principle of virtual works: the case of masonry-like materials as micropolar, second gradient and classical continua. *Acta Mechanica*, 225(1):157–177, 2014.
- [19] D. Bigoni and W. J. Drugan. Analytical Derivation of Cosserat Moduli via Homogenization of Heterogeneous Elastic Materials. *Journal of Applied Mechanics*, 74(4):741–753, 2006.
- [20] Cristina Gatta, Daniela Addessi, and Fabrizio Vestroni. Static and dynamic nonlinear response of masonry walls. *International Journal of Solids and Structures*, 155:291–303, 2018.
- [21] Daniela Addessi and Elio Sacco. Homogenization of heterogeneous masonry beams. *Meccanica*, 53(7):1699–1717, 2018.
- [22] Joung Oh. Chapter 3 - scale effect of the rock joint. In Shuren Wang, Hossein Masoumi, Joung Oh, and Sheng Zhang, editors, *Scale-Size and Structural Effects of Rock Materials*, Woodhead Publishing Series in Civil and Structural Engineering, pages 259–397. Woodhead Publishing, 2020.
- [23] M.J.A. Leal-Gomes. Some New Essential Questions About Scale Effects On the Mechanics of Rock Mass Joints. volume All Days of *ISRM Congress*, 09 2003.
- [24] H. Altenbach and V.A. Eremeyev. *Generalized Continua - from the Theory to Engineering Applications*. CISM International Centre for Mechanical Sciences. Springer Vienna, 2012.
- [25] V.A. Eremeyev, L.P. Lebedev, and H. Altenbach. *Foundations of Micropolar Mechanics*. SpringerBriefs in Applied Sciences and Technology. Springer Berlin Heidelberg, 2012.
- [26] J.L. Ericksen. Special topics in elastostatics††the research work herein reported was supported by a grant from the national science foundation. volume 17 of *Advances in Applied Mechanics*, pages 189–244. Elsevier, 1977.
- [27] J.L. Ericksen. The cauchy and born hypotheses for crystals. In MORTON E. GURTIN, editor, *Phase Transformations and Material Instabilities in Solids*, pages 61–77. Academic Press, 1984.
- [28] Patrizia Trovalusci. *Molecular Approaches for Multifield Continua: origins and current developments*, pages 211–278. Springer Vienna, Vienna, 2014.
- [29] Jean-Jacques Alibert and Alessandro Della Corte. Second-gradient continua as homogenized limit of pantographic microstructured plates: a rigorous proof. *Zeitschrift für angewandte Mathematik und Physik*, 66(5):2855–2870, 2015.
- [30] Meral Tuna, Mesut Kirca, and Patrizia Trovalusci. Deformation of atomic models and their equivalent continuum counterparts using eringen’s two-phase local/nonlocal model. *Mechanics Research Communications*, 97:26–32, 2019.
- [31] Meral Tuna and Patrizia Trovalusci. Scale dependent continuum approaches for discontinuous assemblies: ‘explicit’ and ‘implicit’ non-local models. *Mechanics Research Communications*, 103:103461, 2020.
- [32] M. Bacca, D. Bigoni, F. Dal Corso, and D. Veber. Mindlin second-gradient elastic properties from dilute two-phase cauchy-elastic composites. part i: Closed form expression for the effective higher-order constitutive tensor. *International Journal of Solids and Structures*, 50(24):4010–4019, 2013.
- [33] R. Luciano and J.R. Willis. Bounds on non-local effective relations for random composites loaded by configuration-dependent body force. *Journal of the Mechanics and Physics of Solids*, 48(9):1827–1849, 2000.
- [34] W.J. Drugan and J.R. Willis. A micromechanics-based nonlocal constitutive equation and estimates of representative volume element size for elastic composites. *Journal of the Mechanics and Physics of Solids*, 44(4):497–524, 1996.
- [35] Renato Masiani and Patrizia Trovalusci. Cosserat and cauchy materials as continuum models of brick masonry. *Meccanica*, 31(4):421–432, 1996.
- [36] S Forest, R Dendievel, and G R Canova. Estimating the overall properties of heterogeneous cosserat materials. *Modelling and Simulation in Materials Science and Engineering*, 7(5):829–840, sep 1999.
- [37] Patrizia Trovalusci and Renato Masiani. A multifield model for blocky materials based on multiscale description. *International Journal of Solids and Structures*, 42(21):5778–5794, 2005. PACAM VIII SPECIAL ISSUE.
- [38] Patrizia Trovalusci and V. Sansalone. A numerical investigation of structure-property relations in fiber composite materials. *International Journal for Multiscale Computational Engineering*, 5(2):141–152, 2007.
- [39] Cihan Tekoğlu and Patrick R. Onck. Size effects in two-dimensional voronoi foams: A comparison between generalized continua and discrete models. *Journal of the Mechanics and Physics of Solids*, 56(12):3541–3564, 2008.
- [40] Nicholas Fantuzzi, Patrizia Trovalusci, and Raimondo Luciano. Multiscale analysis of anisotropic materials with hexagonal microstructure as micropolar continua. *International Journal for Multiscale Computational Engineering*, 18(2):265–284, 2020.
- [41] Valeria Settimi, Patrizia Trovalusci, and Giuseppe Rega. Dynamical properties of a composite microcracked bar based on a generalized continuum formulation. *Continuum Mechanics and Thermodynamics*, 31(6):1627–1644, 2019.
- [42] Daniela Addessi and Elio Sacco. Enriched plane state formulation for nonlinear homogenization of in-plane masonry wall. *Meccanica*, 51(11):2891–2907, 2016.
- [43] Daniela Addessi. A 2d cosserat finite element based on a damage-plastic model for brittle materials. *Computers & Structures*, 135:20–31, 2014.
- [44] Nicholas Fantuzzi, Lorenzo Leonetti, Patrizia Trovalusci, and Francesco Tornabene. Some novel numerical applications of cosserat continua. *International Journal of Computational Methods*, 15(06):1850054, 2018.
- [45] I. A. Kunin. *Elastic Media with Microstructure I. One-Dimensional Models*. Springer, 1982.
- [46] Cemal Eringen. *Microcontinuum Field Theories*. Springer, 1999.
- [47] Cemal Eringen. *Nonlocal Continuum Field Theories*. Springer, 2002.
- [48] J. D. Frost and J. Han. Behavior of interfaces between fiber-reinforced polymers and sands. *Journal of Geotechnical and Geoenvironmental Engineering*, 125(8):633–640, 1999.
- [49] Samuel G Paikowsky, Christine M Player, and Peter J Connors. A dual interface apparatus for testing unrestricted friction of soil along solid

- surfaces. *Geotechnical Testing Journal*, 18(2):168–193, 1995.
- [50] Alejandro Martinez and J. Frost. The influence of surface roughness form on the strength of sand–structure interfaces. *Géotechnique Letters*, 7:1–8, 03 2017.
- [51] Babak Ebrahimian, Ali Noorzad, and Mustafa I. Alsaleh. A numerical study on interface shearing of granular cosserat materials. *European Journal of Environmental and Civil Engineering*, 0(0):1–33, 2019.
- [52] Y. Li, J. Oh, R. Mitra, and B. Hebblewhite. A Joint Asperity Degradation Model Based on the Wear Process. volume All Days of *U.S. Rock Mechanics/Geomechanics Symposium*, 06 2015.
- [53] SM Mahdi Niktabar, K Seshagiri Rao, and Amit Kumar Shrivastava. Effect of rock joint roughness on its cyclic shear behavior. *Journal of Rock Mechanics and Geotechnical Engineering*, 9(6):1071–1084, 2017.
- [54] Babak Ebrahimian, Ali Noorzad, and Mustafa I Alsaleh. Modeling interface shear behavior of granular materials using micro-polar continuum approach. *Continuum Mechanics and Thermodynamics*, 30(1):95–126, 2018.
- [55] Matthew S. Dietz and Martin L. Lings. Postpeak strength of interfaces in a stress-dilatancy framework. *Journal of Geotechnical and Geoenvironmental Engineering*, 132(11):1474–1484, 2006.
- [56] Georg Koval, François Chevoir, Jean-Noël Roux, Jean Sulem, and Alain Corfdir. Interface roughness effect on slow cyclic annular shear of granular materials. *Granular Matter*, 13(5):525–540, 2011.
- [57] Carlo Baggio and Patrizia Trovalusci. Collapse behaviour of three-dimensional brick-block systems using non-linear programming. *Structural Engineering and Mechanics*, 10(2):181–195, 08 2000.
- [58] Zdeněk P. Bažant and Pietro Gambarova. Rough cracks in reinforced concrete. *Journal of the Structural Division*, 106(4):819–842, 1980.
- [59] PG Gambarova and C Karakoç. A new approach to the analysis of the confinement role in regularly cracked concrete elements. 1983.
- [60] Joost C. Walraven. Fundamental analysis of aggregate interlock. *Journal of the Structural Division*, 107(11):2245–2270, 1981.
- [61] B. Li, Koichi Maekawa, and H. Okamura. Contact density model for stress transfer across cracks in concrete. *Journal of Faculty of Engineering, The University of Tokyo*, 40:9–52, 02 1989.
- [62] Peter H. Feenstra, René de Borst, and Jan G. Rots. Numerical study on crack dilatancy part i: Models and stability analysis. *Journal of Engineering Mechanics*, 117(4):733–753, 1991.
- [63] Lorenzo Leonetti, Nicholas Fantuzzi, Patrizia Trovalusci, and Francesco Tornabene. Scale effects in orthotropic composite assemblies as micropolar continua: A comparison between weak- and strong-form finite element solutions. *Materials*, 12(5), 2019.
- [64] Nicholas Fantuzzi, Patrizia Trovalusci, and Raimondo Luciano. Material symmetries in homogenized hexagonal-shaped composites as cosserat continua. *Symmetry*, 12(3), 2020.
- [65] António JM Ferreira and Nicholas Fantuzzi. *MATLAB codes for finite element analysis: Solids and Structures, Second edition*. Springer, 2020.
- [66] Marco Colatosti, Nicholas Fantuzzi, Patrizia Trovalusci, and Renato Masiani. New insights on homogenization for hexagonal-shaped composites as cosserat continua. *Meccanica*, pages 1–20, 2021.
- [67] Davide Bigoni and Giovanni Noselli. Localized stress percolation through dry masonry walls. part ii – modelling. *European Journal of Mechanics - A/Solids*, 29(3):299–307, 2010.
- [68] Bt Ladanyi and G Archambault. Simulation of shear behavior of a jointed rock mass. In *The 11th US Symposium on Rock Mechanics (USRMS)*. OnePetro, 1969.
- [69] Joung Oh and Gyo-Won Kim. Effect of opening on the shear behavior of a rock joint. *Bulletin of engineering geology and the environment*, 69(3):389–395, 2010.
- [70] Nicholas Fantuzzi, Patrizia Trovalusci, and Snehith Dharasura. Mechanical behavior of anisotropic composite materials as micropolar continua. *Frontiers in Materials*, 6:59, 2019.